11 From Mott to Cluster Mott: Probing Correlations with RIXS

Markus Grüninger
Insitute of Physics II
University of Cologne

Contents

E. Pavarini and E. Koch (eds.)
Correlated Materials: Methods and Applications
Modeling and Simulation Vol. 16, Forschungszentrum Jülich, 2026
ISBN 978-3-95806-909-1 http://www.cond-mat.de/events/correl26

1 Introduction

Correlated electron systems offer fundamentally interesting physics in exotic quantum phases of matter, and their characteristic excitations weave the rich tapestry of their fascinating properties. To develop a comprehensive understanding of a given compound or phase, it is crucial to examine it from the distinct perspectives offered by various spectroscopic tools. Prominent examples include inelastic scattering of neutrons or of photons, angle-resolved photoemission (ARPES), and optical spectroscopy. Resonant inelastic x-ray scattering (RIXS) is a most powerful experimental technique with unique advantages for studying charge-neutral low-energy excitations [1]. This covers a wide field of magnetic and orbital excitations, phonons (and electron-phonon coupling), density-wave excitations, plasmons, electron-hole continua and excitons, and charge-transfer excitations.[1] To underscore the versatility of RIXS, we focus on the example of spin/orbital excitations in Mott insulators. RIXS has been used to, e.g., determine the dispersions of magnons, paramagnons, orbitons, spin-orbit excitons, and of a two-triplon bound state [7–13], probe the continua of bi-magnons, spinons, and triplons [14–17], detect spin excitations with ΔS^z up to 5 [18, 19], and demonstrate the bond-directional character of magnetic excitations in a proximate Kitaev spin liquid [20], to name but a few.

RIXS is a relatively new addition to the field. This is mainly due to enormous advances in synchrotron light sources and instrumentation, improving, e.g., energy resolution and count rates for soft, tender, and hard x-rays [21–24], but also in theoretical description [1–5]. We use an example from the hard x-ray range. In 2011, RIXS at the Ir L_3 edge ($2p_{3/2}$ to $5d$, 11.2 keV) has been predicted to be promising for probing low-energy excitations of spin-orbit entangled $j = 1/2$ moments in $5d^5$ compounds [25]. First results in 2011 used a resolution $\delta E \approx 1$ eV [26]. In 2012–14, this has been improved to $\delta E = 130$ meV [8], 36 meV [22], 30 meV [9], and 25 meV [10], which is widely used until today. The current record is 10 meV but comes with reduced intensity [27]. Still, there are only two user facilities for high-resolution hard x-ray RIXS.[2]

In these lecture notes, we discuss RIXS on Mott-insulating $4d$ and $5d$ transition-metal compounds with strong spin-orbit coupling. We focus on cluster Mott insulators [28], a new class of materials in which electrons are delocalized over a small cluster, e.g., dimers or tetrahedra, while inter-cluster charge fluctuations are suppressed by Coulomb interactions. Such cluster Mott insulators offer the possibility of tailoring and controlling unconventional quasimolecular magnetic moments and exchange interactions, paving the way for novel phases of quantum matter. RIXS is the ideal tool to study the quasimolecular electronic structure and magnetic moments that are governed by the competition of correlation, intra-cluster hopping, spin-orbit coupling, and crystal field. The excitation energy $\hbar\omega_0$ of local intra-cluster excitations does not show dispersion. Still, the $\mathbf{q}$ dependence is a key feature: Coherent resonant scattering on the cluster sites yields an interference pattern in the $\mathbf{q}$-dependent RIXS intensity that reflects the dynamical structure factor $S(\mathbf{q}, \omega_0)$ of the intra-cluster excitations. This interference pattern provides valuable information on the symmetry and character of the electronic states.

[1] For reviews of RIXS, see [1–5]. RIXS has also been addressed within the Jülich Autumn School [6].

[2] European Synchrotron Radiation Facility (ESRF, Grenoble) and Advanced Photon Source (APS, ANL, USA).

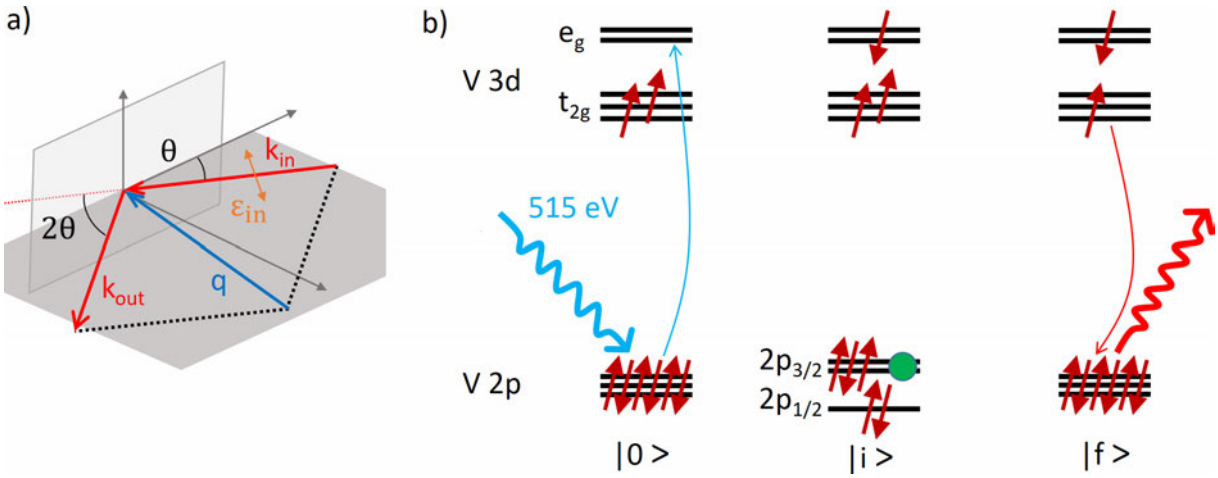

Fig. 1: Resonant inelastic x-ray scattering. *a) Sketch of the scattering geometry with transferred momentum* $\mathbf{q} = \mathbf{k}_{in} - \mathbf{k}_{out}$*, where* 2θ *(not to be confused with* $2 \cdot \theta$*) is the scattering angle and* θ *the angle of incidence. The sketch uses linear incident polarization* ε_{in} *lying in the horizontal scattering plane, while the polarization of the scattered photons is not resolved. b) Example for a direct RIXS process at the V* L_3 *edge at about 515 eV, as observed in* YVO_3 *[29]. In the ground state* $|0\rangle$*, a* V^{3+} d^2 *site hosts two* t_{2g} *electrons with* $S = 1$*. Upon absorption of an x-ray photon with suitable energy* E_{in}*, a* $2p$ *core electron is promoted to the* $3d$ *shell (in this example, we have chosen an* e_g *orbital). At the* L_3 *edge, the intermediate state* $|i\rangle$ *shows a* $2p_{3/2}$ *core hole. Within the* $2p$ *level, spin-orbit coupling is strong, splitting the* $2p^5$ *configuration (*$S = 1/2$*,* $L = 1$*) into* $2p_{1/2}$ *and* $2p_{3/2}$ *states with* $J = 1/2$ *and* $3/2$*, respectively. Finally, an electron relaxes from the* $3d$ *shell to the* $2p$ *core shell and an x-ray photon with energy* E_{out} *is emitted. In the example, the final state* $|f\rangle$ *with excitation energy* $E_{loss} = E_{in} - E_{out}$ *shows a* $t_{2g}^1\, e_g^1$ *state with* $S = 0$*, i.e., a different* $3d^2$ *multiplet. The excitation affects both the orbital occupation and the spin. The change of spin from* $S = 1$ *to 0 is possible since spin is not a good quantum number in the intermediate state with a* $2p_{3/2}$ *core hole. For simplicity, we focused on the transferred energy* E_{loss} *but also the transferred momentum* $\mathbf{q}$ *and the polarizations of incident and scattered photons are relevant.*

The basic principles of RIXS will be introduced in Sec. 2, while Sec. 3 presents an example of resonance behavior. To contextualize the results on cluster Mott compounds, Sec. 4 discusses local cubic multiplets in Mott insulators with strong spin-orbit coupling. We address $5d^3$ K_2ReCl_6 and $5d^4$ K_2OsCl_6, model systems for the competition of Hund's coupling and spin-orbit coupling. In Sec. 5 on cluster Mott insulators, we introduce the concept of RIXS interferometry and demonstrate its power for the study of cluster Mott insulators but also disorder phenomena. In face-sharing $5d$ iridate dimers and trimers, large hopping yields quasimolecular behavior. In an intuitive picture, the quasimolecular orbitals are built from spin-orbit entangled j states. In $4d$ Ru dimers, however, the dichotomy of conventional single-site Mott behavior and quasimolecular cluster Mott insulators breaks down. Hopping, Hund's coupling, and trigonal crystal-field splitting are of comparable size, resulting in an electronic structure with properties that lie between Mott behavior and cluster Mott behavior. Altogether, these compounds provide a new perspective on the competition of hopping and correlations.

2 RIXS on correlated transition-metal compounds

In (R)IXS, an incident x-ray photon with energy E_{in} and wave vector $\mathbf{k}_{\text{in}}$ is absorbed and a photon with E_{out} and $\mathbf{k}_{\text{out}}$ is emitted, see Fig. 1a). This creates[3] an excitation with energy $E_{\text{in}}-E_{\text{out}}$ and $\mathbf{q} = \mathbf{k}_{\text{in}}-\mathbf{k}_{\text{out}}$. For the large x-ray energies such as 11.2 keV at the Ir L_3 edge, the phase space for energy and momentum transfer is huge. With $|q| = (2E_{\text{in}}/\hbar c)\sin(2\theta/2)$, the transferred momentum is as large as, e.g., 8 Å^{-1} for $2\theta = 90°$ and $E_{\text{in}} = 11.2$ keV. For soft x-rays, $|q|$ is smaller, e.g., 0.4 Å^{-1} at the V L_3 edge at 0.51 keV, again for $2\theta = 90°$.

For comparison, we first consider inelastic x-ray scattering (IXS) [30,31]. In *non-resonant* scattering, the x-rays couple to the electronic charge density ρ_c and directly probe the corresponding dynamical structure factor $S_c(\mathbf{q},\omega)$, measuring the fluctuations of ρ_c. IXS is a versatile tool for the study of electron dynamics and phonons, for instance up to 200 meV in graphite [32].[4,5]

In contrast, RIXS is a resonant technique. The incident energy E_{in} is tuned to an x-ray absorption edge, i.e., an atomic transition. Examples are transition-metal K edges (e.g., Cu $1s$ to $4p$), transition-metal L edges (e.g., Cu $2p$ to $3d$), and ligand K edges (e.g., O $1s$ to $2p$).[6] The choice of the absorption edge is decisive for the selection rules, opening entirely different excitation channels and turning RIXS into a most versatile tool. We illustrate this for RIXS at a transition-metal L_3 edge, involving two dipole transitions between $2p$ and d states, see Fig. 1b). The initial absorption process promotes a $2p$ core electron to an empty state in the partially filled d shell, i.e., right into the states relevant to the low-energy properties. Consequently, L-edge RIXS is particularly sensitive to spin and orbital excitations. We choose the case of V $3d^2$ in YVO_3 [29]. The intermediate state shows a $2p^5\,3d^3$ configuration with a $2p$ core hole. The strong potential of the core hole attracts the excited electron, which in the intermediate state does not delocalize in the lattice but is bound to the core-hole site. The intermediate state has a very short life time. It decays via the relaxation of an electron from the $3d$ valence shell to the $2p$ core level, emitting a photon with E_{out}. This leaves the d shell in an excited state $3d^{2*}$. Our example in Fig. 1b) uses an $S=1$ t_{2g}^2 ground state and an $S=0$ $t_{2g}^1\,e_g^1$ final state. Compared to the ground state, the RIXS process created an e_g electron and a t_{2g} hole on the same site, i.e., an on-site exciton, a charge-neutral excitation. In this example, the exciton corresponds to a multiplet excitation in which both the orbital occupation and the total spin have been changed. The change in total angular momentum is balanced by the polarization of the scattered photon.

Thus far, we only referred to local properties, describing a *local* excitation. In fact, the dispersion of orbital excitations is often comparable to the peak width, so that they can be approximated as being local, see Sec. 4.2. However, this is related to the, in many cases, small effective hopping of orbital excitations but is not caused by the RIXS process. Based on the translational invariance of the lattice, the exciton lives in $\mathbf{q}$ space and may delocalize. Propagating orbital excitations with a sizable dispersion are called orbitons and can be observed in RIXS [12]. We

[3] Also annihilation processes with $E_{\text{out}} > E_{\text{in}}$ are possible, equivalent to anti-Stokes Raman scattering.

[4] See [33] for lecture notes of L.H. Tjeng on imaging of orbitals via non-resonant IXS.

[5] In non-resonant IXS, sub-meV resolution has been achieved [34], but RIXS is more challenging, since high resolution has to be realized at the particular energy dictated by the absorption edge of the compound under study.

[6] The K, L, and M edges correspond to core shells with main quantum number $n = 1$, 2, and 3, respectively.

consider the more common case of magnons, propagating spin waves. In a system with long-range magnetic order, a local spin flip is not an eigenstate, but magnons are. A magnon can be viewed as a superposition of local spin flips, and the excitation of a magnon with a given $\mathbf{q}$ corresponds to a coherent sum over spin-flip RIXS processes on all sites involved in the magnon. Since x-rays carry large $\mathbf{q}$, the dispersions of magnons and orbitons can be mapped out.

Spin-flip excitations are allowed in our example of RIXS at a transition-metal L_3 edge [7,25,35]. A spin flip within the d shell is possible due to the strong spin-orbit coupling within the $2p$ shell that splits the core hole states into $2p_{1/2}$ and $2p_{3/2}$, see Fig. 1. The splitting amounts to several eV in $3d$ transition metals such as V or Cu and is as large as 1.6 keV in Ir. Based on this strong spin-orbit coupling, spin is not a good quantum number in the intermediate state. In comparison, spin-orbit coupling vanishes for the $1s$ shell with $L = 0$. Therefore, K-edge RIXS with a $1s$ core hole does not allow for spin-flip excitations [29]. This demonstrates the decisive role of the absorption edge for the selection rules.

All of the RIXS results discussed in the following have been obtained at a transition-metal L edge, using so-called *direct* RIXS as shown in Fig. 1b). Indirect RIXS becomes important when direct RIXS is forbidden by selection rules. As an example for indirect RIXS, we consider the Cu K edge. We start with a dipole transition from the $1s$ core orbital to the *empty* $4p$ valence shell far above the Fermi level, and later the same electron relaxes. The excitation within the partially filled $3d$ shell arises in a shake-up process via the interaction with the core hole in the intermediate state, where the short-lived $4p$ electron can be viewed as a spectator of the physics of the $3d$ shell. For instance, the core hole may be screened by the excitation of a phonon. Thus, phonons can be studied in indirect RIXS, but they are suppressed in direct RIXS [36].

The resonant character of RIXS comes with a series of advantages such as resonant enhancement of the scattering cross section, element and orbital specificity, and control over selection rules. When a solid absorbs an x-ray photon, there are many possible decay channels, and resonant enhancement at an x-ray absorption edge provides a decent signal for low-energy inelastic scattering. At the same time, the choice of a particular absorption edge yields element specificity. Measuring at an absorption edge of a given transition metal, RIXS probes in particular the electronic, orbital, and spin excitations in which ions of this transition-metal element are involved. The dipole selection rules add orbital selectivity that can be controlled via the polarization. Furthermore, the choice of the absorption edge also selects the shell of valence orbitals involved in the intermediate state as well as the selection rules, as discussed above. RIXS at different edges provides different information on the excitations. One example is the comprehensive picture of the crystal-field (or local d-d) and magnetic excitations of the paradigmatic antiferromagnet NiO that has been obtained by studying RIXS at the Ni M, L, and K edges as well as at the O K edge [37–44].

Note that RIXS is a bulk sensitive technique. The x-ray penetration depth depends strongly on the energy and the compound, but it is of the order of 0.1 µm to a few micrometer. Still it is possible to investigate, e.g., thin films, which may require employing a small angle of incidence. Modern synchrotrons are highly brilliant light sources that offer spot sizes down to a few micrometers, permitting the study of small single crystals (order of 100 µm).

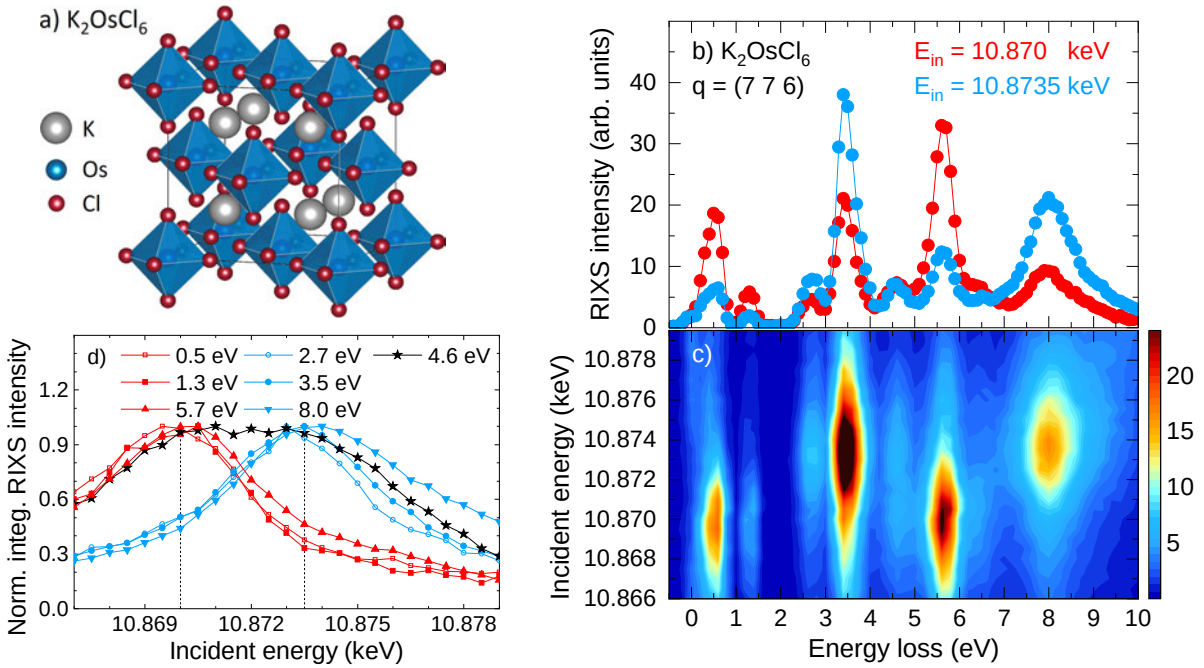

Fig. 2: Resonance behavior of the RIXS intensity at a transition-metal L edge. *We use the $5d^4$ Mott insulator K_2OsCl_6 as an example [45]. Resonant enhancement is revealed by RIXS spectra for a series of incident energies E_{in} across the Os L_3 edge. The energy loss of RIXS peaks is independent of E_{in}. The peak intensity shows resonant enhancement for initial x-ray absorption to either t_{2g} or e_g orbitals at 10.870 keV or 10.8735 keV, respectively. This allows us to distinguish intra-t_{2g} excitations, excitations to e_g orbitals, and charge-transfer excitations. a) Cubic crystal structure of K_2OsCl_6 (space group $Fm\bar{3}m$ at 300 K). b) RIXS spectra measured at t_{2g} and e_g resonance at 20 K. The energy loss axis is the same as for the resonance map in c). d) Normalized cuts through the resonance map at constant loss. The behavior at 4.6 eV indicates two distinct excitations. As shown in a), the $OsCl_6$ octahedra are well separated and form an fcc lattice. The structure can be derived from the widely studied double perovskites $A_2BB'O_6$ by placing ordered vacancies on the B' sites.*

3 Resonance behavior

The resonance behavior is a key feature, as discussed above, and we want to highlight a further aspect: The resonance behavior supports a first peak assignment in the RIXS spectra, a central task in spectroscopy. The Os L_3 edge of the Mott-insulating $5d^4$ antifluorite halide K_2OsCl_6 provides a transparent example [45]. The crystal structure hosts well-separated $OsCl_6$ octahedra, see Fig. 2a), giving rise to well-localized excitations with narrow line widths and thus a particularly clear picture. Figure 2b) shows RIXS spectra for two incident energies $E_{\rm in}$. These spectra are equivalent to cuts through the resonance map shown in Fig. 2c), a color plot being built from RIXS spectra for a series of incident energies across the Os L_3 edge. For all observed peaks, the energy loss $E_{\rm loss} = E_{\rm in} - E_{\rm out}$ is independent of $E_{\rm in}$, demonstrating the excitonic RIXS character of these features with a well-defined excitation energy. This is analogous to Raman scattering with visible light, where the matrix elements depend on the laser frequency but the energy of the Raman peaks does not. This must be distinguished from a fluorescence process in

which the energy loss increases with E_{in}. Consider, e.g., the excitation of an unbound electron-hole pair in a scenario of non-interacting electrons. The core electron may be promoted into a delocalized band state, while the core hole is filled by the decay of an electron from the bottom of the band. In this case, an increase of E_{in} puts the excited electron in a higher-lying band state, while the emission process from the bottom of the band always yields the same energy for the outgoing photons, i.e., the energy loss *increases* with E_{in}. In contrast, in a RIXS process, the energy E_{out} of the emitted photon increases along with E_{in}, reflecting the *constant energy loss* $E_{\text{loss}} = E_{\text{in}} - E_{\text{out}}$ independent of the incident photon energy for a well-defined excitonic excitation such as an on-site orbital d-d excitation or a spin flip.

The data in Fig. 2 reveal a dramatic enhancement of the RIXS signal for incident energies around 10.870 to 10.874 keV. For E_{in} as large as roughly 10^4 eV, it is stunning that the enhancement is restricted to a window of E_{in} of only a few eV, see Fig. 2d). The width of the resonance profile reflects the life time of the intermediate state. For $5d$ L edges in the hard x-ray regime, this life time is of the order of a few femtoseconds only. Note that $3d$ L edges in the soft x-ray range below 1 keV show longer life times and thus even narrower resonance profiles.

Typical for $5d$ transition-metal L_3 edges, K_2OsCl_6 shows two distinct resonance energies that correspond to t_{2g} and e_g resonance. In the absorption step, the $2p$ core electron can be promoted to a t_{2g} or an e_g orbital of the valence d shell, assuming that both subshells contain empty states. In K_2OsCl_6, the two resonance energies equal 10.870 keV and 10.8735 keV. The difference of 3.5 eV provides a rough estimate of the cubic crystal-field splitting $10\,Dq$. We emphasize that the resonance behavior allows for a first peak assignment, i.e., it allows us to distinguish intra-t_{2g} excitations from d-d excitations to e_g orbitals and charge-transfer excitations.

The RIXS peaks below 2 eV show t_{2g} resonance, identifying them as intra-t_{2g} excitations $|t_{2g}^4\rangle \rightarrow |t_{2g}^{4*}\rangle$, see Sec. 4. In cubic symmetry, they are governed by Hund's coupling J_H and spin-orbit coupling ζ, see Sec. 4. Crystal-field or d-d excitations to e_g orbitals are described by $|t_{2g}^4\rangle \rightarrow |t_{2g}^3\, e_g^1\rangle$ in K_2OsCl_6. These additionally involve the cubic crystal-field splitting $10\,Dq$, which above has been estimated as 3.5 eV. Accordingly, excitations to e_g orbitals resonate at a higher E_{in} and show larger energy loss, here 2.7 to 4.6 eV, see Fig. 2. Remarkably, t_{2g} resonance is also observed at higher energy loss, e.g., at 4.6 and 5.7 eV. This marks the onset of charge-transfer excitations from Cl $3p$ to Os $5d$ states, $|5d_{\text{Os}}^4\, 3p_{\text{Cl}}^6\rangle \rightarrow |5d_{\text{Os}}^5 3p_{\text{Cl}}^5\rangle$. The resonance behavior allows us to distinguish $|t_{2g}^5\, 3p_{\text{Cl}}^5\rangle$ final states from $|t_{2g}^4\, e_g^1\, 3p_{\text{Cl}}^5\rangle$ excitations showing e_g resonance, e.g., at 8.0 eV loss. The narrow line widths of the RIXS peaks of K_2OsCl_6 reveal the distinct t_{2g} and e_g resonance behavior of the charge-transfer excitations particularly well.

4 Studying local multiplets of Mott insulators with RIXS

4.1 Cubic multiplets, Hund's coupling, and strong spin-orbit coupling

In Mott insulators, electronic correlations dominate over the kinetic energy gained upon band formation and delocalization. This yields local spin and orbital degrees of freedom, a vast playground for quantum magnetism. In transition-metal compounds with a partially filled d

t_{2g}^n	# states	multiplets	multiplet energies	excitations
1	6	$^2T_2$	0	–
2	$15 = 9{+}3{+}2{+}1$	$^3T_1,\ ^1T_2/^1E,\ ^1A_1$	$U{-}xJ_H\ (x = -3, -1, 2)$	$2J_H, 5J_H$
3	$20 = 4{+}6{+}4{+}6$	$^4A_2,\ ^2T_1/^2E,\ ^2T_2$	$3U{-}xJ_H\ (x = -9, -6, -4)$	$3J_H, 5J_H$
4	$15 = 9{+}3{+}2{+}1$	$^3T_1,\ ^1T_2/^1E,\ ^1A_1$	$6U{-}xJ_H\ (x = -13, -11, -8)$	$2J_H, 5J_H$
5	6	$^2T_2$	$10U{-}20J_H$	–

Table 1: *Overview of local t_{2g}^n multiplets for $n = 1$ to 5 in cubic symmetry [46–48]. The second and third columns give the number of states and the multiplet terms. The dash in, e.g., $^1T_2/^1E$ denotes degenerate states. Multiplet energies are given in the same order as the terms. The prefactor of U counts the number of electron pairs, while the prefactor of J_H depends on the orbital occupation. The last column gives the corresponding energies of on-site excitations.*

shell, the character of the local magnetic moment depends on the electron count but also on Coulomb repulsion, spin-orbit coupling, and crystal-field effects. RIXS directly measures the local multiplet structure, offering a quantitative determination of the electronic parameters and thus the character of the local moments.

To warm up, we consider a single $5d$ transition-metal site and focus on Coulomb interactions in cubic symmetry, while we neglect spin-orbit coupling, non-cubic crystal field, and hybridization with the ligands. The large spatial extent of the $5d$ orbitals produces a large cubic crystal-field splitting, $10\,Dq > 3\,\text{eV}$, as shown above. This motivates the useful and often employed starting point that assumes $10\,Dq \approx \infty$ (Kanamori model). It allows us to neglect e_g orbitals, restricting the discussion to intra-t_{2g} excitations. For the t_{2g} shell, one can quantify Coulomb interactions by two parameters, Hubbard U and Hund's coupling J_H [46–48]. In terms of Coulomb repulsion, it is particularly costly to put two electrons into the same orbital, while it is beneficial if two electrons occupy different orbitals with parallel spins. The corresponding on-site energies are given in Table 1. The configurations t_{2g}^n with $n = 2$, 3, and 4 allow for on-site intra-t_{2g} excitations between Hund's multiplets. The excitation energies depend on J_H but not on U since an on-site excitation changes the orbital occupation but not the local electron count. We will focus on the competition of Hund's coupling and strong-spin-orbit coupling in cubic $5d^3$ and $5d^4$ compounds.

Before discussing the results, we add a note on the value of J_H. For the entire d shell, Coulomb interactions are often parameterized by the Slater-Condon parameters F^0, F^2, and F^4 that correspond to monopole, dipole, and quadrupole contributions.[7] In the t_{2g}-only Kanamori model discussed above, U and J_H are defined as (a comprehensive discussion can be found in [47])

$$U = F^0 + \frac{4}{49}F^2 + \frac{36}{441}F^4, \qquad J_H = \frac{3}{49}F^2 + \frac{20}{441}F^4\,. \tag{1}$$

However, if one considers the entire d shell including the e_g orbitals in the model and the analysis, i.e., for finite $10\,Dq$, one finds different expressions,

$$U_d = F^0, \qquad J_{H,d} = \frac{1}{14}(F^2{+}F^4)\,. \tag{2}$$

[7] Equivalently, one may employ the Racah parameters $A = F^0 - \frac{49}{441}F^4$, $B = \frac{1}{49}F^2 - \frac{5}{441}F^4$, $C = \frac{35}{441}F^4$.

Typically, a fixed ratio F^4/F^2 is considered,[8] often $F^4/F^2 \approx 5/8$. This yields

$$J_H \approx 0.77 J_{H,d} \,. \tag{3}$$

The numerical value of Hund's coupling depends on the model used. A comparison of both models has been reported for $5d^4$ K_2OsCl_6 and $5d^3$ K_2ReCl_6 [45, 49]. An analysis of the RIXS data of K_2OsCl_6 that considers the entire $5d$ shell yields $F^2 = 3.7$ eV, $F^4 = 2.2$ eV, and $J_{H,d} = 0.43$ eV. Equation (3) predicts $J_H \approx 0.33$ eV, in reasonable agreement with an analysis restricted to the t_{2g} states, giving $J_H \approx 0.28$ eV [45] (see below). The t_{2g}-only model may yield reasonable results, but it is important to indicate the model to which one refers.

In recent years, the rich physics originating from strong spin-orbit coupling combined with electronic correlations has attracted enormous interest [28, 50–54]. In $5d$ transition-metal compounds, spin-orbit coupling is comparable to Hund's coupling. Therefore, spin and orbital degrees of freedom are strongly entangled, and the resulting effective total angular momentum states differ qualitatively from conventional spin states. This is the basis for multipolar order in $5d^1$ and $5d^2$ compounds [55], excitonic magnetism in $5d^4$ and $4d^4$ materials [56], and experimental realizations of Kitaev-type bond-directional exchange interactions in, e.g., $5d^5$ $j{=}1/2$ compounds [20, 57, 58]. In passing, we note that $5d^5$ $j{=}1/2$ K_2IrCl_6 has been discussed as a nodal-line spin liquid [59] and as an example for the entanglement not only between spins and orbitals but also with lattice degrees of freedom [36, 60]. Below, we address $5d^4$ K_2OsCl_6, providing an exceptionally clean realization of the non-magnetic $J{=}0$ state induced by strong spin-orbit coupling, and the effect of spin-orbit coupling on a half-filled shell in $5d^3$ K_2ReCl_6 [45,49].

4.2 $5d^4$ configuration: Non-magnetic $J{=}0$ K_2OsCl_6

Excellent model systems for spin-orbit-entangled quantum states can be found in the Mott-insulating antifluorite transition-metal halides A_2MX_6 with K_2PtCl_6-type structure. These compounds exist for a wide variety of tetravalent metal ions (M = Pt, Re, Os, and Ir, etc.) for A = K, Rb, Cs, or $(NH)_4$, and X = F, Cl, Br, and I. The isolated MX_6 octahedra (see Fig. 2a)) suppress direct metal-metal hopping and thereby favor localized behavior. This structural simplicity facilitates a direct comparison between experimental spectra and atomic multiplet calculations. Furthermore, at room temperature these compounds show a cubic crystal structure [61–63], allowing us to focus on the interplay of Hund's coupling J_H and spin-orbit coupling ζ for the case where the two coupling constants are comparable in size. This intermediate regime is located between the LS coupling limit realized for $\zeta/J_H \to 0$ and the jj coupling regime[9] that corresponds to $\zeta/J_H \to \infty$.

The t_{2g}^4 configuration has attracted considerable interest in the context of *excitonic magnetism* [56, 64]. Starting from a local non-magnetic $J = 0$ ground state, strong exchange interactions between neighboring sites may cause a sizable dispersion of the $J = 1$ excited state such that this

[8] Another common choice is Racah $C/B = 4$, equivalent to $F^4/F^2 = 36/55$.

[9] In LS coupling, the total angular momentum J of an ion is calculated by coupling the total spin S and the total angular momentum L, where both S and L are obtained by summing over the electrons. In contrast, in jj coupling, l and s of each electron are first coupled to j before J is calculated by summing over the electrons.

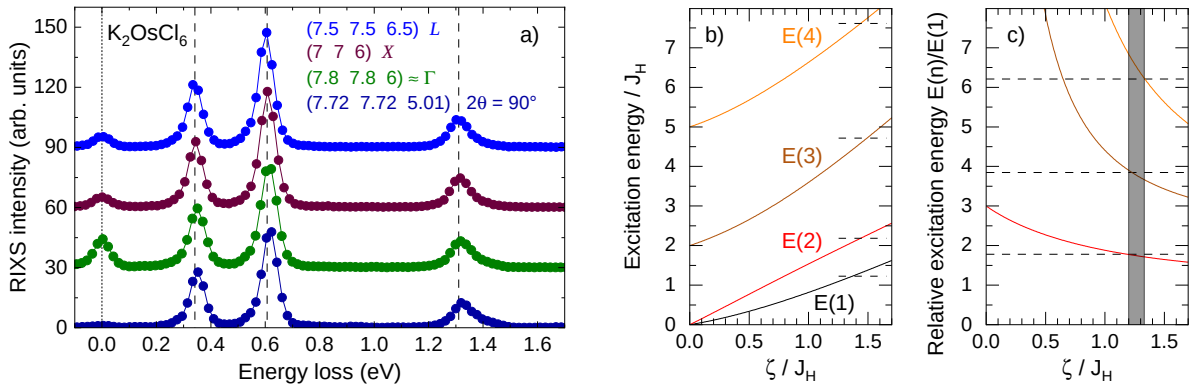

Fig. 3: Intra-t_{2g} excitations of K_2OsCl_6. *a) RIXS spectra at selected* $\mathbf{q}$ *points show local excitations at 0.34, 0.61, and 1.31 eV with negligible* $\mathbf{q}$ *dependence [45]. Dashed: peak energies at the* X *point. A fourth peak has been detected at 2.1 eV [45]. The elastic line is weak since a scattering angle* 2θ *close to 90° has been used along with incident* π *polarization. Full suppression of the elastic line is achieved for* $2\theta = 90°$ *(dark blue), in which case the polarization of the scattered x-rays is perpendicular to the incident* π *polarization. The data, plotted with a vertical offset, have been collected at 20 K in the tetragonal phase. The energy resolution of 63 meV is not sufficient to resolve the non-cubic splitting of 4 meV observed in infrared data [45]. b) Effect of spin-orbit coupling on the excitation energies* $E(1)$ *to* $E(4)$ *in the* t_{2g}*-only Kanamori model. Dashed: experimental results assuming* $J_H = 0.28$ *eV. c) Ratios of excitation energies* $E(n)/E(1)$ *as a function of* ζ/J_H*. Dashed: experimental values. Grey:* $\zeta/J_H = 1.20$–1.33.

magnetic state may condense, yielding a magnetic ground state. The key signature of excitonic magnetism is a magnetic amplitude mode equivalent to a Higgs mode that has been discussed for antiferromagnetic Ca_2RuO_4 [56,65]. However, layered Ca_2RuO_4 shows a sizable non-cubic crystal-field splitting $\Delta_{\rm CF}$ larger than ζ. Therefore, the magnetism of t_{2g}^4 Ca_2RuO_4 can also be described using a low-energy $S=1$ model with anisotropy, and the pros and cons of the two approaches, starting from $J=0$ or $S=1$, have been discussed extensively [48, 65–70].

For K_2OsCl_6, Fig. 3a) shows the low-energy RIXS spectra for selected $\mathbf{q}$ points [45]. An energy resolution $\delta E = 63$ meV has been achieved at the Os L_3 edge, i.e., $\delta E/E_{\rm in} \approx 6\cdot 10^{-6}$. The spectra show intra-t_{2g} excitations at about 0.34, 0.61, and 1.31 eV. Note that the error bar of the energy of a well-separated peak is smaller than δE. Within the experimental resolution, the peak energies do not depend on the transferred momentum $\mathbf{q}$. The absence of dispersion underpins the local character of these excitations. The excitation energies agree very well with the results obtained from infrared spectroscopy for $\mathbf{q}\approx 0$ [45]. A further RIXS peak has been observed at 2.1 eV [45]. This intra-t_{2g} mode is another example of the important role of selection rules [71]. Its RIXS intensity vanishes for a scattering angle of $90°$, which is often chosen experimentally to suppress the contribution of the elastic line at zero energy loss, see Fig. 3a).

Above we have discussed the limit of $10\,Dq = \infty$ with spin-orbit coupling $\zeta = 0$. The neglect of the e_g orbitals can be motivated by the large value of $10\,Dq \approx 3.5$ eV and by the resonance behavior, see Sec. 3. For the t_{2g}^4 configuration, Coulomb interactions yield a nine-fold degenerate $^3T_1$ ground state and excited states at $2J_H$ and $5J_H$, see Table 1. However, the experimental data show more than two peaks as spin-orbit coupling splits the $^3T_1$ multiplet into the $J=0$

ground state, the $J = 1$ triplet, and the $J = 2$ quintuplet. The five t_{2g}^4 energies are given by [72]

$$E_{J=0\,/\,^1A_1} = \frac{5}{2} J_H \left(1 \mp \sqrt{1 + \frac{2}{5}\frac{\zeta}{J_H} + \left(\frac{3}{5}\frac{\zeta}{J_H}\right)^2} \right) - \frac{\zeta}{2} \tag{4}$$

$$E_{J=1} = -\frac{\zeta}{2} \tag{5}$$

$$E_{J=2\,/\,(^1T_2/^1E)} = \frac{2}{2} J_H \left(1 \mp \sqrt{1 - \frac{1}{2}\frac{\zeta}{J_H} + \left(\frac{3}{4}\frac{\zeta}{J_H}\right)^2} \right) + \frac{\zeta}{4}\,. \tag{6}$$

The corresponding excitation energies $E(1)$ to $E(4)$, relative to $E_{J=0}$, are depicted in Fig. 3b) as a function of ζ/J_H. Fitting the four intra-t_{2g} excitation energies observed in RIXS yields $J_H \approx 0.28$ eV and $\zeta/J_H \approx 1.45$. The dashed lines in Fig. 3b) indicate the experimental peak energies for $J_H = 0.28$ eV. These results firmly establish that K_2OsCl_6 is located in the intermediate regime between LS coupling and jj coupling.

This claim is supported by the ratios $E(n)/E(1)$ for $n = 2$ to 4, which yield $\zeta/J_H = 1.20$–1.33, see Fig. 3c). A discussion of relative excitation energies may be favorable for comparison with other d^4 compounds. We focus on the ratio $E(2)/E(1)$. For $\zeta/J_H \to 0$ (LS coupling), one finds $E(1) \approx 0.5\zeta$ and $E(2) \approx 1.5\zeta$, see Eqs. (4) to (6). For $\zeta/J_H \to \infty$ (jj coupling), $E(1) \approx E(2) \approx 1.5\zeta$. The ratio $E(2)/E(1)$ changes from 3 to 1 between the two limits, see Fig. 3c). In K_2OsCl_6, $E(2)/E(1) \approx 1.8$ marks the intermediate regime. RIXS results on $5d^4$ iridates [73–76] show very similar ratios $E(2)/E(1)$, pointing to similar values of ζ/J_H.

The t_{2g}-only Kanamori model offers a reasonable description of the intra-t_{2g} excitation energies. With the assumption $10\,Dq = \infty$, it is not surprising that the agreement with the experimental data is not perfect. Taking into account the e_g orbitals with finite $10\,Dq$ has clear consequences: it lifts the degeneracy of the $J = 2$ quintuplet as well as the degeneracy of the $^1T_2$ and ^1E multiplets [45]. For $J = 2$, the effect is too small to be resolved in our RIXS data. Regarding $^1T_2$ and ^1E, the RIXS peak at 1.31 eV exhibits an asymmetric line shape with a high-energy shoulder, see Fig. 3a). Infrared data of K_2OsCl_6 confirm a peak splitting [45]. A combined analysis of RIXS and infrared data considering the entire d shell yields $\zeta_d = 0.34$ eV and $J_{H,d} = 0.43$ eV, equivalent to $\zeta_d/J_{H,d} \approx 0.8$ [45]. The different definitions of J_H and $J_{H,d}$ have been discussed above, see Eqs. (1) and (2). We emphasize that the choice of the model also affects the value of the spin-orbit coupling constant, $\zeta \neq \zeta_d$. Beyond the degeneracies discussed above, the Kanamori model and a model considering the entire d shell achieve a similar level of agreement with the intra-t_{2g} excitation energies observed in $5d^4$ K_2OsCl_6 [45]. However, the analytic expressions of the energies in the Kanamori model, see Eqs. (4)–(6), simplify the analysis considerably.

4.3 $5d^3$ K_2ReCl_6: spin-orbit coupling in a half-filled shell

The role of spin-orbit coupling in the case of a half-filled t_{2g} shell is an interesting conceptual question. In the LS coupling limit, the three electrons maximize the total spin according to Hund's rule, giving rise to a spin-only $S = 3/2$ scenario with quenched orbital momentum. Based

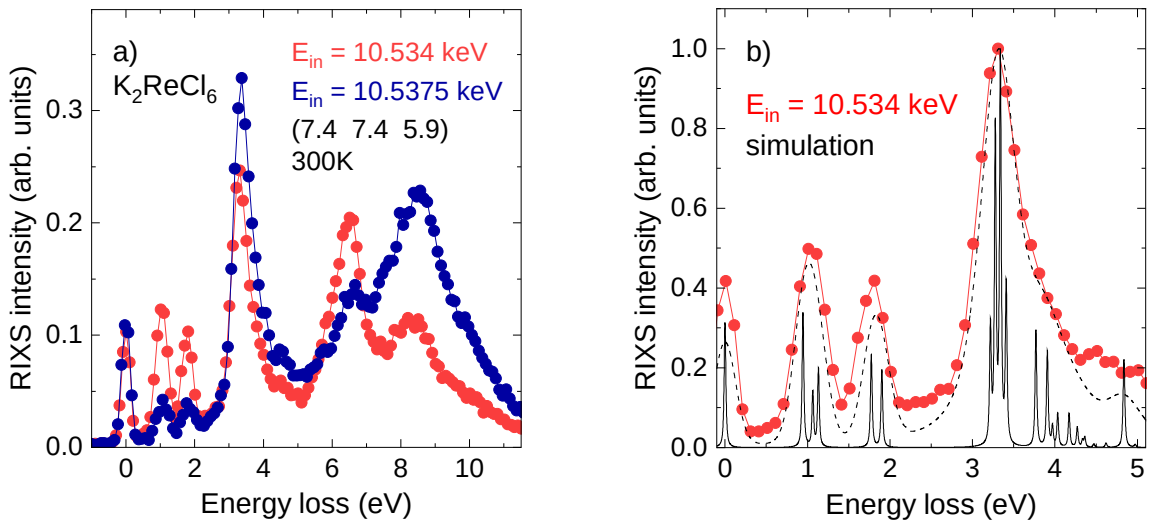

Fig. 4: RIXS spectra of cubic $5d^3$ K_2ReCl_6 [49]. *a) The data have been measured at 300 K with 295 meV resolution for incident energy E_{in} = 10.534 keV (t_{2g} resonance) and 10.5375 keV (e_g resonance). Intra-t_{2g} peaks are observed at 1.0 and 1.8 eV, while excitations to e_g states are peaking at 3.3 eV. b) Comparison of RIXS data (red) with a simulated spectrum (black) calculated for 10 Dq = 3.25 eV, ζ_d = 290 meV, and $J_{H,d}$ = 464 meV. Solid: Voigt oscillators with 10 meV line width. Dashed: same data with larger line width.*

on the equal occupation of the three t_{2g} orbitals, a distortion does not lower the energy. This spin-only scenario describes, e.g., the gapless magnetic excitations reported for $4d^3$ Ca_3LiRuO_6 [77]. Streltsov and Khomskii [53] pointed out that this well-known scenario breaks down for large ζ/J_H in the jj coupling limit. For $\zeta/J_H \to \infty$, the electrons occupy states with $j = 3/2$ and $1/2$ character. The half-filled t_{2g} shell corresponds to a 3/4-filled $j = 3/2$ quartet, allowing for a Jahn-Teller splitting of the t_{2g}^3 configuration [53], in stark contrast to the spin-only $S = 3/2$ scenario. It is intriguing to consider how the many-body states evolve as a function of ζ. In the intermediate-coupling regime, the entanglement of spin and orbital angular momenta gives rise to anisotropy and the opening of a spin gap. In fact, sizable spin gaps have been reported for, e.g., $5d^3$ Ca_3LiOsO_6 and Ba_2YOsO_6 [78–81], which have been discussed in terms of a spin-orbit-entangled $J = 3/2$ state [82]. Antifluorite K_2ReCl_6 is an ideal model system for examining the competition of strong spin-orbit coupling and Hund's coupling in a cubic crystal field with only small interactions between adjacent sites.

Thus far, RIXS at the Re L_3 edge has hardly been studied. The resonant character of RIXS is a major experimental challenge because the setup has to be optimized for every absorption edge to be studied. For hard x-rays, this affects in particular the energy resolution δE as one has to choose an analyzer crystal with an appropriate Bragg peak for energy discrimination. Figure 4 shows RIXS spectra of cubic $5d^3$ K_2ReCl_6 with $\delta E = 295$ meV for incident energies that correspond to t_{2g} resonance and e_g resonance, respectively [49].

Equivalent to the case of $5d^4$ K_2OsCl_6, cf. Fig. 2, the resonance behavior of $5d^3$ K_2ReCl_6 reveals the intra-t_{2g} character of the RIXS peaks at 1.0 and 1.8 eV, strong excitations from $|t_{2g}^3\rangle$ to $|t_{2g}^2 e_g^1\rangle$ around 3.5 eV, and charge-transfer excitations from the ligand Cl p shell to either Re

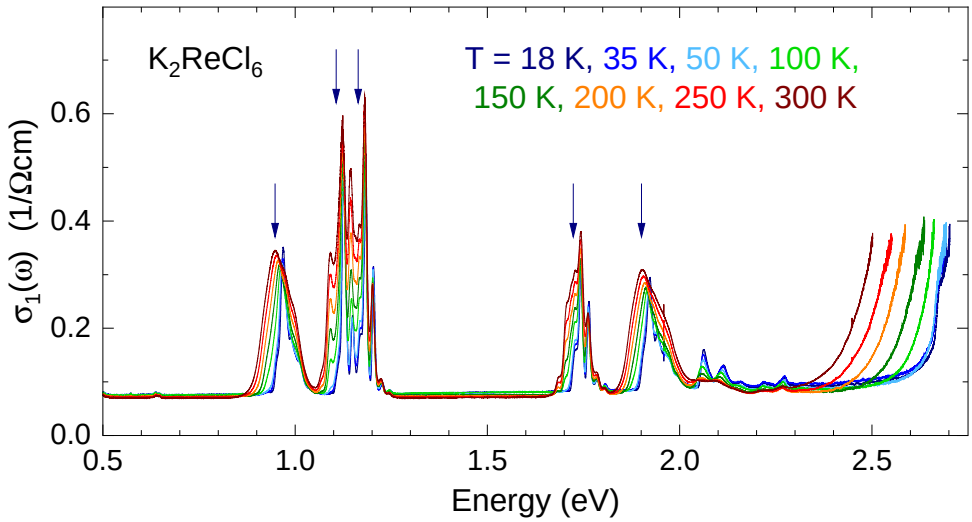

Fig. 5: Intra-t_{2g} excitations in the optical conductivity $\sigma_1(\omega)$ of $5d^3$ K_2ReCl_6. *RIXS shows two peaks at 1.0 and 1.8 eV, cf. Fig. 4. The infrared data resolve all five on-site d-d excitations between 0.9 and 2 eV (arrows). In $\sigma_1(\omega)$, the d-d exitations are both parity forbidden and spin forbidden but acquire a small spectral weight in a phonon-assisted process with a characteristic temperature dependence. The rich line shape is caused by vibronic sidebands, i.e., electron-phonon coupling. These weak absorption features can only be detected below the Mott gap, the onset of which is observed at 2.7 eV at low temperature. The even weaker peaks between 2.0 and 2.3 eV correspond to pair excitations of intra-t_{2g} excitations on neighboring sites [49].*

t_{2g} or e_g orbitals above 5 eV. Based on Coulomb interactions, assuming $10\,Dq = \infty$ and $\zeta = 0$, one expects a $S = 3/2$ $^4A_2$ ground state and intra-t_{2g} excitations at $3J_H$ and $5J_H$, see Table 1. Assuming $\zeta = 0$, the excitation energies 1.0 and 1.8 eV suggest $J_H \approx 0.35$ eV. Both spin-orbit coupling and finite $10\,Dq$ yield a peak splitting that we cannot resolve in RIXS with 295 meV resolution, see Fig. 4b). Four RIXS peaks have been reported in $5d^3$ Ca_3LiOsO_6 and Ba_2YOsO_6 with $\delta E = 150$ meV [82]. Infrared data of K_2ReCl_6 resolve all five intra-t_{2g} excitations [49].

For the study of local d-d excitations, RIXS and infrared spectroscopy are complementary in terms of selection rules and energy resolution [49]. On-site d-d excitations are allowed in L-edge RIXS [1], see Fig. 1. In contrast, infrared absorption is predominantly sensitive to electric dipole excitations such as inter-site excitations across the Mott gap. In the presence of inversion symmetry, d-d excitations are parity forbidden in optical spectroscopy. However, a finite matrix element arises in a phonon-assisted process, where inversion symmetry is broken by the simultaneous creation or annihilation of an odd-symmetry phonon. This gives rise to weak phonon-assisted d-d excitations [36, 45, 49, 83, 84]. Note that the peak energies in RIXS and optical data are shifted by the phonon energy, and that the phonon-assisted nature of the process leaves its fingerprints in a characteristic temperature dependence of the spectral weight and line shape of the optical data. In K_2ReCl_6, the spectral weight in infrared data is further suppressed by the spin-selection rule, which can be relaxed by spin-orbit coupling.

Weak phonon-assisted d-d excitations can be detected in infrared transmittance measurements on single crystals. This requires that the weak excitations are located in a transparent frequency

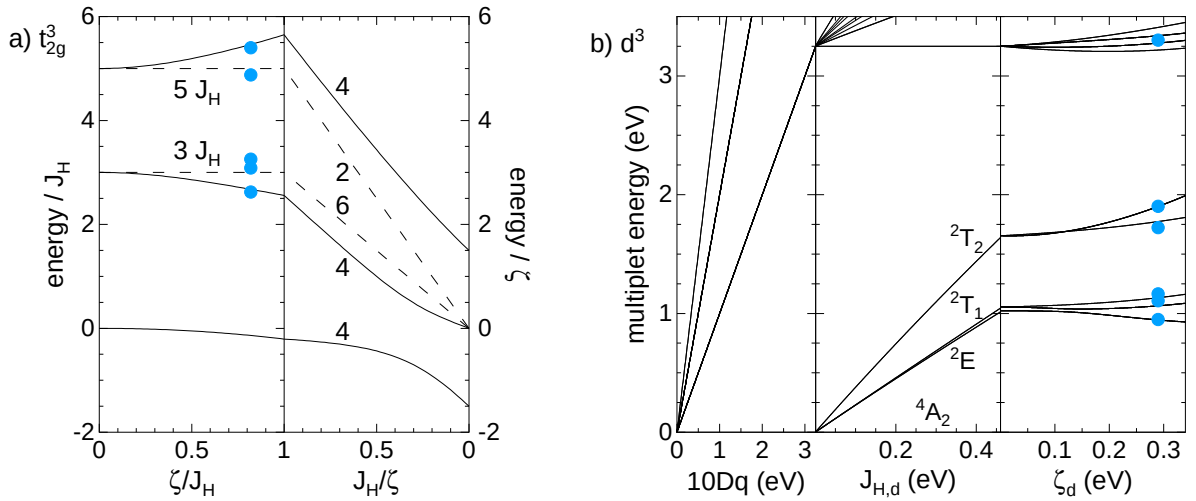

Fig. 6: Energies for the d^3 configuration in cubic symmetry [49]. *a) Absolute energies of the t_{2g}^3 states in the Kanamori model for $10Dq = \infty$, see Eq. (7). Spin-orbit coupling mixes the states plotted with solid lines, giving rise to in total four excitation energies relative to the ground state. The energies are shown from $\zeta/J_H = 0 \to \infty$. Note the change of scale of both axes. Blue symbols show the experimental result for $\zeta/J_H = 0.82$ with $J_H = 343$ meV. Numbers in the right panel denote the degeneracy. b) Energy level diagram including e_g states for finite $10Dq$. The panels show the excitation energies upon consecutively switching on the cubic crystal-field splitting $10Dq$, Hund's coupling $J_{H,d}$, and spin-orbit coupling ζ_d. The energies have been calculated using* QUANTY *[88, 89]. Blue symbols depict the experimental results for the five intra-t_{2g} excitation energies and the t_{2g}-to-e_g RIXS peak at 3.3 eV.*

range with no strong absorption features, e.g., between the phonons and the Mott gap. In this range, infrared data of K_2ReCl_6 reveal five phonon-assisted absorption bands with a multitude of vibronic phonon sidebands,[10] see Fig. 5. These phonon sidebands must be distinguished from the symmetry-breaking phonon mode of the phonon-assisted process. For K_2ReCl_6, a thorough analysis yields the five electronic excitation energies 948, 1107, 1164, 1723, and 1901 meV [49], resolving the splitting of the RIXS peaks observed at 1.0 and 1.8 eV.

We start from the t_{2g}-only Kanamori model with $10\,Dq = \infty$ in cubic symmetry, which describes four of the five excitation energies. The Kanamori model fails to capture the distinct energies of the two states at 1107 and 1164 meV. The eigenstates for finite ζ are described by comparably simple analytic expressions [49, 85, 86]. The absolute energies $E(i)$ for $i = 0$ to 4 are plotted in Fig. 6a) and in ascending order are given by (for $n \in \{0, 1, 2\}$) [49]

$$E(0) = E_0, \quad E(1) = E_2, \quad E(2) = 3J_H, \quad E(3) = E_1, \quad E(4) = 5J_H, \tag{7}$$

$$\frac{E_n}{J_H} = \frac{8}{3} - \frac{\tau}{3} \cdot \cos\left[\frac{1}{3}\arccos\left(\frac{4(284-3\tau^2)}{\tau^3}\right) + 2\pi\frac{n}{3}\right], \qquad \tau = 2\sqrt{19 + 3\left(\frac{3}{2}\frac{\zeta}{J_H}\right)^2}.$$

The four excitation energies result after subtracting the ground-state energy $E(0)$. Finite ζ splits the excitations at $3J_H$ and $5J_H$. For intermediate coupling with $\zeta/J_H \approx 1$, this splitting is of the

[10] In L-edge RIXS, such vibronic sidebands have been resolved in $5d^5$ K_2IrCl_6 [36].

order of $\zeta/2$. In the limit of jj coupling, the ground state shows all three electrons in $j=3/2$ states, and one can excite one or two electrons to $j=1/2$ with respective excitation energies $3\zeta/2$ and 3ζ. Reasonable agreement between experiment and Kanamori model is obtained for $\zeta/J_H \approx 0.8$ with $J_H = 343$ meV [49], see blue symbols in Fig. 6a). We conclude that K_2ReCl_6 is in the intermediate-coupling regime, similar to K_2OsCl_6. Spin-orbit coupling ζ is sizable but not large enough for a description in terms of jj coupling.

Spin-orbit coupling mainly mixes the Jahn-Teller-active $^2T_2$ multiplet into the ground state. However, the admixture increases only $\propto (\zeta/J_H)^2$. A significant Jahn-Teller effect requires strong spin-orbit coupling $\zeta/J_H \gtrsim 1.5$ [53]. In K_2ReCl_6 with $\zeta/J_H \approx 0.8$, the expectation value $\langle L_z \rangle \approx (1/25)(\zeta/J_H)^2 \approx 0.027$ is still very small and more than 97 % of the ground-state weight is contributed by the $S=3/2$ $^4A_2$ multiplet [49]. This agrees with a Curie-Weiss analysis of the magnetic susceptibility [87], which finds an effective magnetic moment $\mu_{\text{eff}} \approx 3.81\,\mu_B$ that is close to the value $2\sqrt{S(S+1)}\,\mu_B \approx 3.87\,\mu_B$ expected for a $S=3/2$ compound.

For the excitation energies, the agreement between experiment and theory can be improved by considering the entire $5d$ shell, including the e_g orbitals. This in particular explains the peak splitting around 1.1 eV. In K_2ReCl_6, infrared spectroscopy detects the intra-t_{2g} excitations with high accuracy, but it cannot resolve the on-site d-d excitations to e_g states with energies above the Mott gap, see Fig. 5. However, the t_{2g}-to-e_g excitations give a strong peak at 3.3 eV in RIXS. The combination of RIXS and optical spectroscopy is a most powerful tool for studying multiplets in Mott insulators. Together, these techniques provide a comprehensive picture of the electronic structure, enabling quantitative extraction of microscopic parameters. Figure 6b) gives the on-site d^3 excitation energies for a model for the entire d shell. The first panel depicts the effect of the cubic crystal field, $10\,Dq$, and the second panel shows the splitting of the cubic multiplets by Coulomb interactions. The ^2E and $^2T_1$ multiplets are degenerate in the Kanamori model, but this degeneracy is lifted by finite $10\,Dq$ even for $\zeta = 0$. The third panel shows the effect of spin-orbit coupling, which finally yields five intra-t_{2g} excitation energies. A fit of the five experimental intra-t_{2g} excitation energies and of the energy of the RIXS peak at 3.3 eV yields $10Dq = 3.25$ eV, $\zeta_d = 290$ meV, and $J_{H,d} = 464$ meV (with $F^2 = 3.93$ eV and $F^4/F^2 = 36/55$), see symbols in Fig. 6b). For these parameters, a RIXS spectrum calculated with QUANTY [88, 89], using the experimental resolution 295 meV, agrees very well with the experimental data, see Fig. 4b).

5 Cluster Mott insulators

We now switch from conventional Mott insulators to Mott-insulating materials with lattices containing small clusters such as dimers, trimers, or tetramers. Cluster Mott insulators are a novel class of transition-metal compounds in which electrons are delocalized over, e.g., individual dimers due to strong *intra*-cluster hopping t [28, 90–97], cf. Figs. 7a) and 8a). Intra-cluster hopping dominates over Coulomb repulsion, but Coulomb wins against *inter*-cluster hopping. A set of dimers with one orbital per site is the most simple example. In the limit of large intra-dimer hopping, quasimolecular bonding and antibonding orbitals are formed. With, e.g., one

electron per dimer, the lattice of dimers hosts a half-filled band of bonding orbitals. A cluster Mott insulator may arise for sufficiently small inter-dimer hopping such that Coulomb repulsion suppresses inter-cluster charge fluctuations.

In Sec. 4, we addressed conventional Mott insulators and discussed how the electronic multiplets depend on the competition of Hund's coupling and spin-orbit coupling. In a Mott insulator, virtual inter-site hopping processes yield exchange interactions. In a cluster Mott insulator, the "local" physics is much richer. One may hope that this is also valid for the exchange couplings generated by inter-cluster hopping. In, e.g., iridate dimers, the magnetic moments were predicted to be anisotropic and temperature dependent due to the existence of low-energy electronic states [98]. In general, the quasimolecular magnetic moments are determined by Coulomb interactions, spin-orbit coupling, crystal fields, and intra-cluster hopping. This yields a multitude of cluster states with the possibility of tuning the character of the magnetic moments [91, 92, 94], as discussed below. The ultimate goal of such tuning is to engineer the interactions between quasimolecular moments to realize novel magnetic phases such as quantum spin liquids.

For a dimer in the limit of strong hopping, the electrons are delocalized in (anti-)bonding orbitals. However, also the conventional Mott limit can be realized on a dimer, with electrons that are localized on individual sites experiencing exchange coupling. This limit requires strong electronic correlations dominating over intra-cluster hopping. RIXS is well suited to distinguish these two limits and demonstrate the quasimolecular electronic structure of cluster Mott insulators [90–94, 99–101]. Moreover, RIXS can quantify the competition of hopping, correlations, spin-orbit coupling, and crystal-field splitting, even in the intriguing crossover regime when both hopping and correlations are relevant [94].

5.1 RIXS interferometry

For an intuitive picture, we start from *non-resonant elastic* x-ray scattering, a standard tool for studying the crystal structure. Bragg peaks result from interference of the scattered x-rays, i.e., from a coherent sum over scattering events on all lattice sites. Now consider *resonant* elastic scattering. For an incident photon energy at, e.g., the Ir L edge, the signal mainly stems from scattering on Ir ions and, to good approximation, can be derived by coherently summing over Ir sites only. In RIXS, *resonant inelastic* scattering, we have to coherently sum all the paths that lead from the ground state $|0\rangle$ to a given excited state $|f\rangle$. If this excited state is delocalized over – and restricted to – a dimer, the corresponding scattering events can occur only on the two Ir sites of this dimer. More precisely, at the Ir L edge, the intermediate state shows a $2p$ core hole (cf. Fig. 1) on either of the two Ir sites. Summing coherently over the corresponding scattering events yields two-beam interference of the scattered x-rays, see Fig. 7c), causing a sinusoidal intensity modulation $I(\mathbf{q})$ that is equivalent to an inelastic incarnation of Young's double-slit experiment. For dimers, sinusoidal modulation of the RIXS intensity was predicted in the mid 90's [99, 100] and observed in 2019 [90]. At the L edge, the two "slits" effectively correspond to Ir $2p$ core levels that are involved in the intermediate state of the RIXS process. With a size of a few picometers, they can be considered as nearly point-like, providing a nearly constant

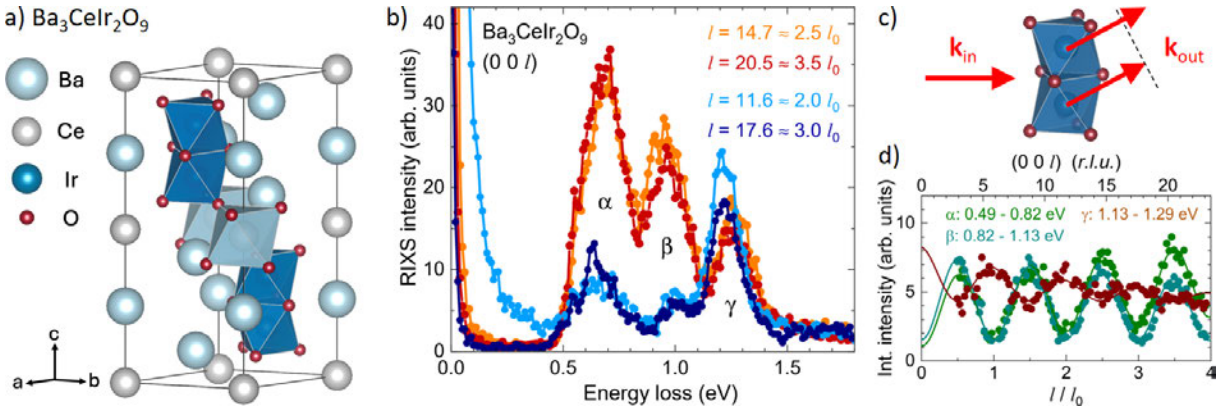

Fig. 7: RIXS on the two-hole dimer $Ba_3CeIr_2O_9$ [90]. *a) Crystal structure of $Ba_3CeIr_2O_9$ with dimers built from face-sharing IrO_6 octahedra. The intra-dimer Ir-Ir distance is given by d. b) L_3-edge RIXS spectra at selected $\mathbf{q}$ points, measured at 20 K with 27 meV resolution. The peak intensities vary strongly with $\mathbf{q}$. The strong intensity of the elastic line at (0 0 11.6) (light blue) reflects a scattering angle far away from 90°. c) Two-beam interference for RIXS on a dimer. d) Integrated intensities of the three RIXS peaks for a wide range of q_c, the component of $\mathbf{q}$ parallel to the dimer axis. The top (bottom) axis shows q_c in units of $2\pi/c$ ($l_0 = 2\pi/d$). The two peaks below 1.1 eV agree with $\sin^2(q_c d/2)$ behavior, the third peak predominantly shows $\cos^2(q_c d/2)$ modulation, cf. Eq.* (10).

envelope for the intensity modulation.[11] This is important since it allows us to study the RIXS interference pattern over a very large range of $\mathbf{q}$, e.g., 20 Brillouin zones in Fig. 7d). We call this approach RIXS interferometry.

For a single dimer, the RIXS intensity for excitation from the ground state $|0\rangle$ to an excited state $|f\rangle$ with the excitation energy $\hbar\omega_f$ is given by

$$I(\mathbf{q},\omega) = |A_f(\mathbf{q})|^2\, \delta(\omega - \omega_f)\,, \tag{8}$$

where[12] $A_f(\mathbf{q})$ is the coherent sum of the amplitudes of all possible scattering processes on the two dimer sites giving rise to the excitation $|f\rangle$. This sum is the source of the interference. In a crystal, any dimer may be excited. In the total RIXS intensity, this yields an *incoherent* sum over all dimers, summing the intensities (not the amplitudes) of all dimers. A cluster shows discrete excitation energies without dispersion. Nevertheless, the RIXS intensity strongly depends on $\mathbf{q}$. Calculating the amplitude $A_f(\mathbf{q})$ is significantly simplified in the fast-collision approximation [1], which in the hard x-ray range is often appropriate for direct RIXS processes due to the very short core-hole lifetime of only a few femtoseconds. In this case, the amplitude can be split into a resonant prefactor and the dynamical structure factor $S(\mathbf{q},\omega_f)$. For constant incident energy, the former can be neglected. In the dipole approximation, this yields [1]

$$A_f(\mathbf{q}) \sim \left\langle f \middle| \sum_{\mathbf{R}} e^{i\mathbf{q}\mathbf{R}} \left[D^\dagger(\epsilon_{\text{out}}^*) D(\epsilon_{\text{in}})\right]_{\mathbf{R}} \middle| 0 \right\rangle, \tag{9}$$

[11] This is similar to neutron scattering on nuclei. In contrast, the form factor for magnetic neutron scattering depends on the more extended magnetization density, so that the intensity is suppressed with increasing $\mathbf{q}$.

[12] The amplitude also depends on the incident energy and the polarizations of incident and scattered photons [1].

where $\mathbf{R}$ runs over all sites over which the final state $|f\rangle$ is delocalized, D denotes the local dipole transition operator, and ϵ_{in} and ϵ_{out} give the polarization of incident and scattered photons, respectively. For simplicity, we consider a dimer with $\mathbf{R}_{1,2} = (0, 0, \pm d/2)$, i.e., Ir-Ir distance d. In the presence of inversion symmetry, the eigenstates show either even or odd parity, and the dipole matrix elements on the two sites may only differ by sign. The coherent sum over resonant scattering processes on the two dimer sites yields

$$I_+(\mathbf{q}) \sim (e^{i\mathbf{q}\mathbf{R}_1} + e^{i\mathbf{q}\mathbf{R}_2})^2 \sim \cos^2(q_c d/2), \qquad I_-(\mathbf{q}) \sim (e^{i\mathbf{q}\mathbf{R}_1} - e^{i\mathbf{q}\mathbf{R}_2})^2 \sim \sin^2(q_c d/2), \quad (10)$$

where q_c denotes the z component of $\mathbf{q}$ parallel to the dimer axis, while I_+ (I_-) applies to excitations that preserve (flip) parity. The $\mathbf{q}$-dependent RIXS intensity thus contains a structural fingerprint of the cluster, here the intra-dimer distance d. Moreover, important information on the symmetry and character of the electronic states is encoded in the $\cos^2(q_c d/2)$ vs. $\sin^2(q_c d/2)$ behavior. The original elastic version of Young's double-slit experiment shows the $I_+(\mathbf{q})$ modulation since the final state and initial state are identical. In contrast, in RIXS an excitation from, e.g., an even-parity bonding state to an odd-parity anti-bonding state is described by $I_-(\mathbf{q})$, essentially providing information on the relative phase of the wavefunction on the two sites.
In summary, the interference pattern directly probes the wave function of cluster Mott insulators and carries information on the symmetry and character of the quasimolecular electronic states [90–95]. It is straightforward to extend the concept to larger clusters such as trimers [93] (see below) or tetrahedra [92]. Related studies of modulated RIXS intensities have been reported for, e.g., homonuclear diatomic molecules such as O_2 [5, 102], the magnetic excitations of the van der Waals ferromagnet $Fe_{4.75}GeTe_2$ [103], and in the context of witnessing entanglement [104, 105]. A sinusoidal intensity modulation can also be observed for magnetic excitations when magnetic correlations along a given direction are restricted to pairs of nearest neighbors, e.g., in bilayers [106, 107] or Kitaev materials [20].

5.2 Face-sharing $5d$ iridates: dimers, trimers, and disorder phenomena

A cluster Mott insulator is based on strong intra-cluster hopping. This is realized in, e.g., $5d$ transition-metal compounds with MO_6 octahedra in face-sharing geometry found in the large family of hexagonal perovskites [108]. In, e.g., $Ba_3CeIr_2O_9$, the intra-dimer Ir-Ir distance d is about 2.5 Å, see Fig. 7a), shorter than in Ir metal. The analysis of our RIXS data yields direct hopping of the order of 1 eV [90]. An attractive feature of the family of $6H$-perovskites $Ba_3MIr_2O_9$ is that it allows for M ions with different valence, e.g., Ta^{5+}, Ce^{4+}, In^{3+}, or Ca^{2+}. Thus, iridate dimers can be realized with one to four t_{2g} holes and different magnetic moments. Related dimers with even larger t_{2g} hole counts exist, e.g., in the $4d$ ruthenates $Ba_3MRu_2O_9$.
The non-magnetic dimer compound $Ba_3CeIr_2O_9$ hosts Ir^{4+} ions. The Ir^{4+} t_{2g}^5 configuration with a single t_{2g} hole per site is well known for the formation of local spin-orbit-entangled $j = 1/2$ moments. In a Mott picture, the non-magnetic character would result from strong antiferromagnetic exchange within a dimer, causing a singlet ground state. In a cluster Mott scenario, the two holes fill a bonding orbital, see Fig. 8b). Spectroscopic measurements can tell the difference. In

L_3-edge RIXS, the $j = 1/2$ moments have a clear fingerprint: the excitation to $j = 3/2$ at $1.5\,\zeta$, about 0.6 to 0.7 eV. The three-peak structure of the RIXS spectra of $Ba_3CeIr_2O_9$ is clearly different, see Fig. 7b), pointing to a cluster Mott picture. Indeed, the $\mathbf{q}$ dependence firmly establishes the quasimolecular character. The RIXS peaks do not show a dispersion, but their intensity strongly depends on $\mathbf{q}$. Figure 7d) shows the integrated intensities $I(q_c)$ of the three RIXS peaks over a very wide range of q_c, spanning roughly 20 Brillouin zones. The period of the interference pattern equals $2\pi/d$, being incommensurate with the size of the Brillouin zone $2\pi/c$. The two peaks below about 1.1 eV reveal a $\sin^2(q_c d/2)$ behavior, while the third peak at 1.2 eV is of $\cos^2(q_c d/2)$ type. This pinpoints the electrons (or holes) being delocalized over a given dimer and provides valuable information on the character of the excitations.

A dimer built from face-sharing IrO_6 octahedra shows mirror symmetry but breaks inversion symmetry. This mixes even- and odd-parity states such that the RIXS intensity for a single dimer follows $I(q_c) \propto [\alpha \sin(q_c d/2) + \beta \cos(q_c d/2)]^2$. However, the crystal structure shows two dimer orientations, rotated by π around the dimer axis, see Fig. 7a). Adding the RIXS intensities of the two orientations yields $I_{\text{tot}}(q_c) \propto [\alpha \sin(q_c d/2)]^2 + [\beta \cos(q_c d/2)]^2$, a sinusoidal modulation with a finite offset [90]. The data demonstrate sinusoidal behavior over a very wide range of q with only a small change of amplitude, i.e., with a slowly varying envelope. This reflects the nearly point-like nature of the $2p$ core hole, as mentioned above. The envelope is hardly affected by the negligible "slit width" but reflects polarization effects, since a change of q requires a change of the scattering geometry, see Fig. 1a). Thus, α and β effectively vary with $\mathbf{q}$.

Now we address the quantitative analysis. The dimer structure with a 3-fold rotation axis splits the t_{2g} orbitals into the a_{1g} and e_g^π orbitals, see Fig. 8a), quantified by Δ_{trig}. Hopping is diagonal in the a_{1g}-e_g^π basis and forms the corresponding (anti-)bonding states, see top panel of Fig. 8b). Assuming that strong hopping suppresses the role of spin-orbit coupling, the quasimolecular ground state is approximated as a spin singlet with the two holes in the bonding a_{1g} orbital. In the opposite limit of strong spin-orbit coupling, we start from local $j = 1/2$ and $3/2$ states. In this picture, hopping yields (anti-)bonding j states, see bottom panel of Fig. 8b). Note that hopping is diagonal in the j basis for $t_{e_g^\pi}/t_{a_{1g}} = -1$ but not for realistic ratios $t_{e_g^\pi}/t_{a_{1g}} \approx -1/2$. Still, the ground state in this picture hosts both holes in a spin-orbit-entangled bonding orbital, $J = 0$ instead of $S = 0$. The electronic parameters allow us to tell which of the two limits is closer to reality. A thorough comparison of the RIXS data with model calculations – considering only the t_{2g} states – yields $t_{a_{1g}} = 1.1$ eV, $t_{e_g^\pi} = -0.5$ eV, $U = 1.0$ eV, $J_H = 0.3$ eV, spin-orbit coupling $\zeta = 0.45$ eV, and the trigonal crystal-field splitting $\Delta_{\text{trig}} = -0.2$ eV [90]. This parameter set quantifies the quasimolecular character. In the Mott limit with dominant Coulomb repulsion, each dimer site carries one hole, and virtual hopping processes mediate exchange couplings. With increasing hopping, states with the two holes on the same site are more and more mixed into the ground state. In the quasimolecular limit of dominant hopping, the two holes occupy a bonding orbital. In this limit, the ground state shows equal weights of states with one hole per site or with double occupancy. For the parameters determined for $Ba_3CeIr_2O_9$, these weights are plotted in the left panel of Fig. 8c) as a function of $t_{a_{1g}}$ (for fixed $t_{e_g^\pi}/t_{a_{1g}} = -0.45$). The weight of states with double occupancy already increases strongly for small $t_{a_{1g}}$ and reaches more than

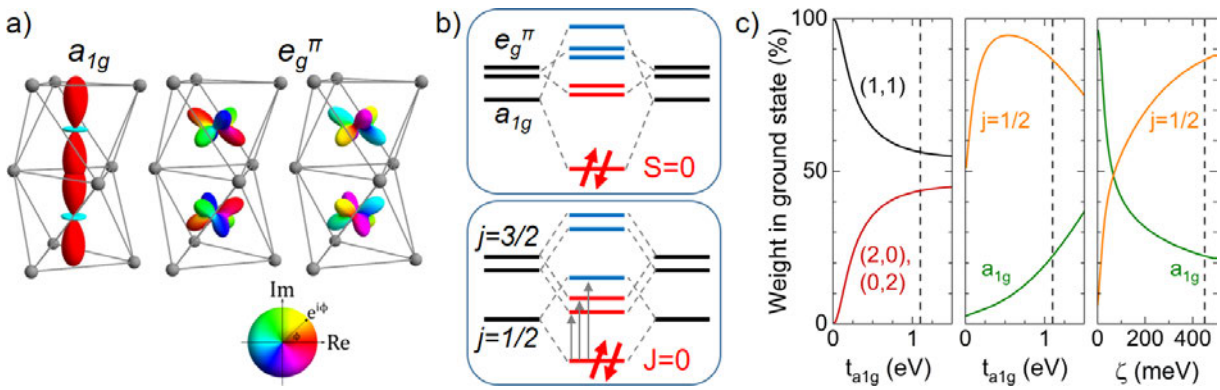

Fig. 8: Quasimolecular electronic structure of a two-hole dimer [90]. *a)* t_{2g} *orbitals in trigonal symmetry:* a_{1g} *and* e_g^π *orbitals. The color code depicts the phase. For face-sharing dimers, hopping is diagonal in the* a_{1g}*-*e_g^π *basis. b) In the limit of large hopping, a non-interacting picture is appropriate, where hopping forms bonding (red) and anti-bonding orbitals (blue). Top: Neglecting spin-orbit coupling* ζ*, two holes occupy the bonding* a_{1g} *orbital in the ground state. Bottom: For strong* ζ*, the quasimolecular (anti-)bonding orbitals originate from spin-orbit-entangled* j *states. This picture correctly describes the* $\sin^2$ *vs.* $\cos^2$ *interference patterns of the three RIXS peaks (grey arrows; cf. Fig. 7), providing an intuitive picture of the physics. c) Weights of contributions to the ground state wavefunction. Left: In the Mott limit for* $t_{a_{1g}} \to 0$*, each site hosts one hole (black). With increasing hopping, the contribution of states with double occupancy increases (red). Both curves extrapolate to 50 % for* $t_{a_{1g}} \to \infty$*. Dashed:* $t_{a_{1g}} = 1.1$ *eV, highlighting the quasimolecular character. Middle and right: Weights for the two holes being either in the bonding* $j = 1/2$ *orbital or in the bonding* a_{1g} *orbital. The latter dominates for* $t_{a_{1g}} \gtrsim 2$ *eV or for small* ζ*. For realistic parameters, the ground state is well approximated by two holes occupying the bonding* $j = 1/2$ *orbital. The plots use the parameters found for* $Ba_3CeIr_2O_9$ *(*$t_{a_{1g}} = 1.1$ *eV,* $t_{e_g^\pi}/t_{a_{1g}} = -0.45$*,* $U = 1.0$ *eV,* $J_H = 0.3$ *eV,* $\zeta = 0.45$ *eV,* $\Delta_{trig} = -0.2$ *eV), scanning either* $t_{a_{1g}}$ *or* ζ*.*

40 % for realistic hopping. This provides a quantitative foundation for the quasimolecular description of $Ba_3CeIr_2O_9$ and for using the single-particle-like pictures of (anti-)bonding orbitals in Fig. 8b). Hopping is so large that correlations do not play a prominent role for a single dimer. However, correlations still suppress inter-cluster charge fluctuations.

Comparing quasimolecular states of a_{1g} and spin-orbit entangled j character, the latter provide a better basis for an intuitive understanding. With $\zeta \approx 0.4$–0.5 eV, spin-orbit coupling is a decisive factor even for large hopping. For the ground state, the middle and right panels of Fig. 8c) plot the weights of states with double occupancy of the bonding a_{1g} or bonding $j = 1/2$ orbitals. In the limit of extreme intra-cluster hopping, the compound is a band insulator with a filled band of bonding a_{1g} states. However, for $t_{a_{1g}} = 1.1$ eV, the occupation of the bonding a_{1g} orbital is reduced to roughly 20 %. In contrast, in the j basis, double occupancy of the bonding $j = 1/2$ orbital describes about 85 % of the ground state. Interestingly, the quasimolecular j states already dominate for ζ larger than 0.1 eV, see right panel of Fig. 8c). The scenario of quasimolecular j states also provides an intuitive description of the observed q dependence. The two lowest RIXS peaks are assigned to excitations to bonding orbitals originating from $j = 3/2$ states. These are split by Δ_{trig}, J_H, and the hopping ratio $t_{e_g^\pi}/t_{a_{1g}} \neq -1$. In contrast, the third

peak corresponds to the excitation to an anti-bonding state, see vertical grey arrows in Fig. 8b). This agrees with the $\sin^2$ modulation of the lower two peaks and the $\cos^2$ behavior of the third.

Dimers with an odd number of holes: An odd number of holes yields a magnetic moment, underscoring the important role of spin-orbit coupling. For different hole counts, phase diagrams have been discussed as a function of ζ and U (for fixed J_H/U) [98]. We restrict ourselves to a brief discussion of the three-hole dimer compound $Ba_3InIr_2O_9$. It exhibits persistent spin dynamics down to 20 mK [109] and thus has been discussed as a promising spin-liquid candidate. A quantitative understanding of the magnetic moments is a prerequisite for discussing magnetism. Using RIXS interferometry, the quasimolecular nature has been established for $Ba_3InIr_2O_9$ [91]. The central aspect is that, with three holes per dimer, the actual character of the magnetic moments can be tuned via the size of hopping. In the ground state, two holes fill the bonding $j=1/2$ orbital but the orbital occupied by the third hole depends on the electronic parameters. It occupies the anti-bonding $j=1/2$ orbital for small hopping, but the bonding $j=3/2$ orbital for larger hopping. The value of hopping thus determines the character of the quasimolecular magnetic moment. The compound $Ba_3InIr_2O_9$ is found to be very close to this phase transition, on the large-hopping side [91, 98]. This is a simple example for a highly promising feature of cluster Mott insulators: in general, the magnetic moments may be tunable via electronic parameters.

Disorder: Disorder may have an unusual effect on magnetism in cluster Mott insulators. Substituting a magnetic ion in, e.g., a dimer by a nonmagnetic one does not create a simple vacancy but changes the magnetic moment of this dimer from quasimolecular to single-site type, which also affects the exchange interactions. RIXS interferometry is very well suited to disentangle the different local moments in a disordered system and to assign the excitations to different transition-metal sites, as shown for $Ba_3Ti_{3-x}Ir_xO_9$ [95], see Fig. 9. The sister compound $Ba_3CeIr_2O_9$, discussed above, shows perfect cation ordering, with the Ir ions occupying the $4f$ sites and the much larger Ce ions the $2a$ sites. In $Ba_3Ti_{3-x}Ir_xO_9$, a strong Ti-Ir site disorder is caused by the comparable ionic radii of the Ir^{4+} and Ti^{4+} ions [110]. This allows for x different from 2 with Ir and Ti ions randomly distributed over the $4f$ and $2a$ sites [95]. With strong site disorder, the discussions of $Ba_3Ti_{3-x}Ir_xO_9$ as a spin-liquid candidate [111–113] must be reconsidered.

Counterintuitively, the average magnetic moment of $Ba_3Ti_{3-x}Ir_xO_9$ *decreases* as the concentration x of magnetic Ir^{4+} ions increases [112]. This can be rationalized via the coexistence of non-magnetic quasimolecular Ir_2 dimers (see $Ba_3CeIr_2O_9$) and single-site Ir^{4+} $j=1/2$ moments, where the relative contribution of non-magnetic dimers increases with increasing x. For small x, the Ir ions are diluted throughout the lattice. For $x=0.3$, RIXS data show a narrow peak at 0.57 eV, roughly $1.5\,\zeta$, revealing the presence of individual $5d^5$ Ir^{4+} sites, see Fig. 9a). This so-called spin-orbit exciton corresponds to the local excitation from the $j=1/2$ ground state to a $j=3/2$ excited state, which has also been observed in K_2IrCl_6 [36] and many other $5d^5$ iridates. In $Ba_3Ti_{3-x}Ir_xO_9$, the shoulder at 0.7 eV is caused by the non-cubic crystal field. For large $x=1.5$ or 1.8, the presence of dimers yields further RIXS features, but the narrow peak

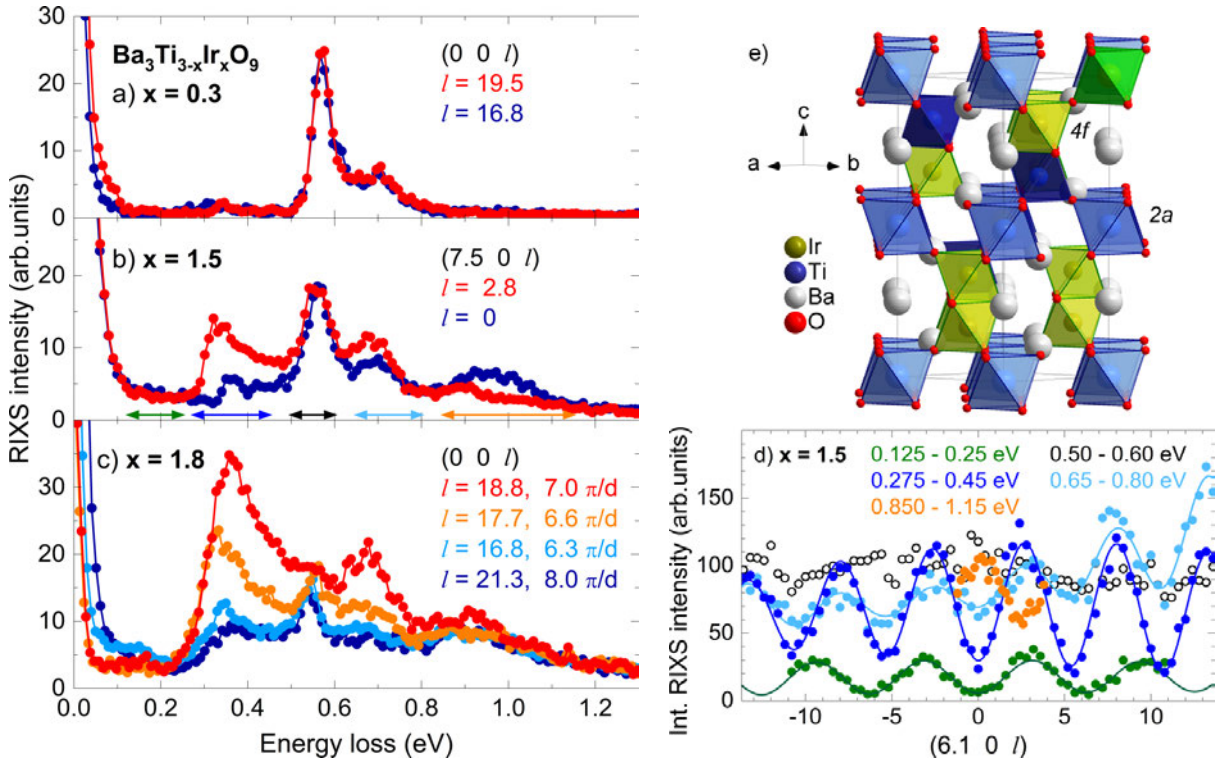

Fig. 9: Strong Ti-Ir site disorder in $Ba_3Ti_{3-x}Ir_xO_9$ [95]. *a)-c) RIXS spectra for $x = 0.3$, 1.5, and 1.8 at 20 K. d) Integrated RIXS intensity for $x = 1.5$. The corresponding energy ranges are marked by arrows in b). We find three types of excitations: (i) The narrow peak of the spin-orbit exciton is the hallmark feature for individual $j = 1/2$ sites. The RIXS intensity of this single-site excitation does not depend on* $\mathbf{q}$ *but may show some polarization dependence (black dots in d)). (ii) Quasimolecular face-sharing Ir_2 dimers (4f sites) contribute broad peaks above 0.2 eV with sinusoidal intensity modulation. (iii) Exchange-coupled Ir 2a-4f pairs yield a magnetic excitation at 0.15 eV, which is revealed by the larger period of the interference pattern. e) Sketch of the crystal structure, cf. Fig. 7a). Ti-Ir site disorder yields Ir ions on 2a sites (green) and Ti ions on 4f dimer sites (dark blue). This produces 2a-4f pairs and single Ir^{4+} $j = 1/2$ moments.*

of the spin-orbit exciton prevails, demonstrating that individual $j = 1/2$ sites are still present. For all x, the 0.57 eV peak does not show any $\mathbf{q}$ dependence, neither in excitation energy nor in intensity, see Fig. 9a)-d), clearly establishing its local, single-site character.

The RIXS spectra reveal the crossover from predominant $j = 1/2$ sites for small x to mainly dimers for x closer to 2. For $x = 1.5$ and 1.8, the three broad RIXS peaks at about 0.35, 0.7, and 0.95 eV can be assigned to excitations on dimers. This is firmly established by the sinusoidal $\mathbf{q}$ dependence of the integrated RIXS intensity, see Fig. 9d). The lower two peaks show $\sin^2(q_c d/2)$ behavior (blue and light blue), while a $\cos^2(q_c d/2)$ response is observed around 0.95 eV (orange). This is fully equivalent with the results discussed for $Ba_3CeIr_2O_9$ with RIXS peaks at 0.7, 1.0, and 1.2 eV. The reduced energy scale in $Ba_3Ti_{3-x}Ir_xO_9$ roughly can be attributed to the larger intra-dimer Ir-Ir distance $d \approx 2.65$ Å [110] compared to 2.54 Å for M = Ce. A larger d yields a smaller bonding-antibonding splitting. Note that $d = 2.65$ Å agrees with the observed period of approximately $5.3 \times 2\pi/c$, see Fig. 9d).

The power of RIXS interferometry to unravel disorder phenomena is most evident from the analysis of the weak feature at 0.15 eV found for large x. Its integrated RIXS intensity (green symbols in Fig. 9d)) shows a sinusoidal two-site interference pattern. However, the period is about 17 % larger, corresponding to a distance of (2.26±0.03) Å projected onto the c axis. This agrees with the projected distance of 2.22 Å between the $2a$ and $4f$ sites reported in x-ray diffraction at 300 K [110]. The interference pattern thus pinpoints the nature of the 0.15 eV peak. Induced by Ti-Ir site disorder, it corresponds to a magnetic excitation of Ir pairs with one Ir ion on a $2a$ site and one on a $4f$ dimer site. The $2a$ and $4f$ sites are also displaced *perpendicular* to c, and the assignment is corroborated by the observation of the corresponding intensity modulation for $\mathbf{q}$ within the ab plane [95]. The excitation energy of 0.15 eV can be explained by considering two $j = 1/2$ moments with strong Heisenberg exchange via a 180° Ir-O-Ir bond, equivalent to the case of square-lattice Sr_2IrO_4 with magnon energies up to 0.2 eV [8, 10]. Note the difference between a pair of exchange-coupled local moments and quasimolecular orbitals. Compared to face-sharing octahedra, hopping t is much smaller for a 180° bond (corner-sharing geometry). In this case, Coulomb repulsion U suppresses a quasimolecular character, giving rise to two $j = 1/2$ moments with exchange coupling $J \propto t^2/U$. In RIXS, the magnetic excitation of such a spin pair also yields a two-site interference pattern. A stunning example of this has been found for the magnetic excitations of the Kitaev-compound Na_2IrO_3 with spin-spin correlations that are restricted to two nearest-neighbor sites [20].

Trimers: Stacks of face-sharing MO_6 octahedra also yield linear trimers with large hopping, see Fig. 10c). An example is $Ba_4AM_3O_{12}$ with M = Mn, Ru, Rh, and Ir, where the valence of the A ions controls the hole count [108, 114–117]. Based on *ab initio* calculations, a transition from localized electrons for $3d$ Mn to quasimolecular behavior for $5d$ Ir has been suggested [118]. However, the results reported for different compounds paint a vivid picture. Unconventional behavior is found in $4d$ $Ba_4Nb_{1-x}Ru_{3+x}O_{12}$, covering the range from a quantum spin liquid to a heavy-fermion strange metal [114]. The three-hole trimer $Ba_4Ir_3O_{10}$ has been claimed to host a quantum spin liquid down to 0.2 K with a very large frustration parameter and spinon-like excitations observed in RIXS [119, 120]. Interestingly, the discussion favors exchange-coupled $j = 1/2$ moments over a quasimolecular scenario. In contrast, for the three-hole trimer $Ba_5CuIr_3O_{12}$ a quasimolecular picture with covalency-driven collapse of spin-orbit coupling has been claimed [121]. In fact, it has often been assumed that the role of spin-orbit coupling is suppressed for large hopping. Also $Ba_4NbIr_3O_{12}$ with nonmagnetic Nb^{5+} ions and two t_{2g} holes per Ir trimer has been discussed as a spin-liquid candidate [115–117]. With two holes per three sites, it is hard to motivate a conventional Mott insulator. In a quasimolecular picture, however, the two holes occupy a bonding orbital, giving rise to a non-magnetic ground state.

Trimers of face-sharing IrO_6 octahedra exhibit inversion symmetry. In a single-particle picture, hopping yields bonding, non-bonding, and antibonding states, see Fig. 10a). Bonding and antibonding states show even parity, but non-bonding states acquire a minus sign upon inversion. The wavefunction of a non-bonding state has no weight on the central trimer site and opposite phases on the two outer sites, see Fig. 10c), such that the energy of non-bonding orbitals is

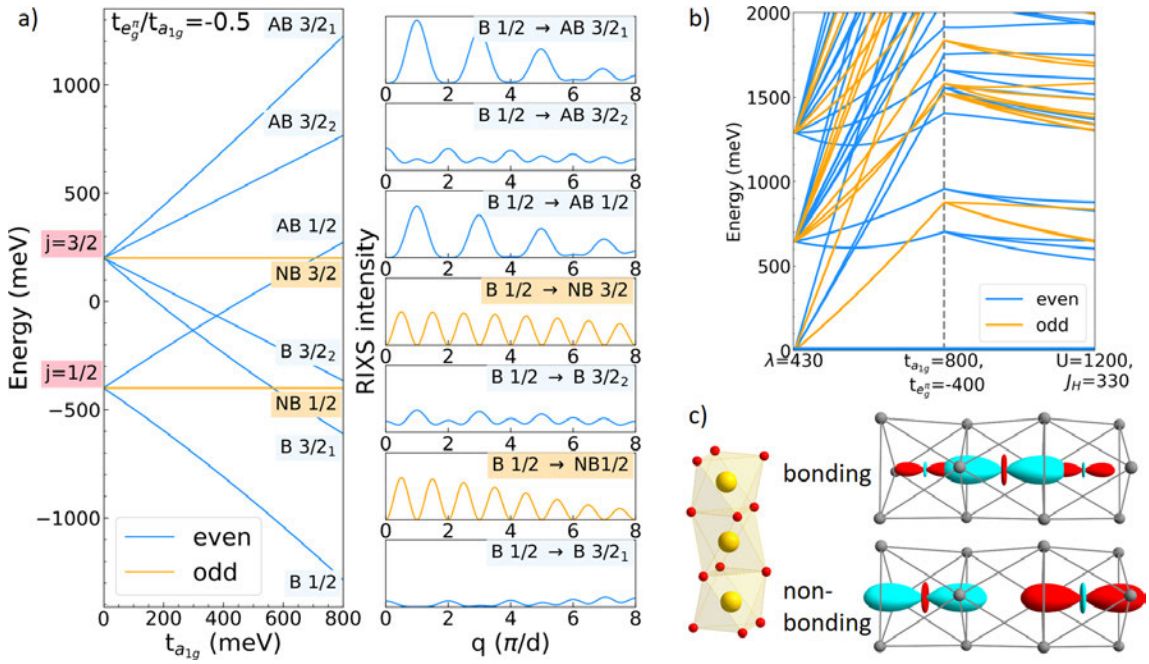

Fig. 10: Quasimolecular states of a linear trimer [93]. *a) Absolute energies of electronic states in a single-particle picture, calculated by exact diagonalization. The energies are given as a function of $t_{a_{1g}}$ for $t_{e_g^\pi}/t_{a_{1g}}$ = -1/2 in the idealized case of cubic crystal field. For $t_{a_{1g}}$ = 0, spin-orbit coupling yields j = 1/2 and 3/2 states split by 1.5 ζ. Hopping yields even-parity (anti-) bonding states (blue) and odd-parity non-bonding states (orange). The finite splitting of the bonding j = 3/2 states reflects that hopping is not diagonal in the j basis (also the antibonding j = 3/2 states are split). Still, a description in terms of j = 1/2 and 3/2 states provides a valid, intuitive picture. Right panel: Calculated RIXS intensity for excitations from the bonding j = 1/2 state to all other levels. The interference patterns reveal the symmetry of the involved states, see Eq.* (11)*. b) Excitation energies for a two-hole trimer for ζ = 0.43 eV, assuming octahedral site symmetry. In the left panel, $t_{a_{1g}}$ increases to 0.8 eV, as in a), such that the ground state shows two holes in the bonding j = 1/2 orbital. For strong hopping, switching on the correlations has only a minor effect (right panel). c) Left: Linear trimer of face-sharing IrO_6 octahedra. The central Ir site is a center of inversion. Right: Simple example for (non-)bonding states in the case of a_{1g} orbitals, highlighting the essential symmetry properties.*

independent of hopping. Evaluating Eq. (9) for a trimer, we find that the modulation pattern of the RIXS intensity of a given excitation is sensitive to the parity of the states involved [93],

$$I_{eo}(q_c) \sim |\alpha|^2 \sin^2(q_c d)\,, \qquad I_{ee}(q_c) \sim |\beta|^2 \cos^2(q_c d) + \gamma \cos(q_c d) + |\delta|^2\,, \tag{11}$$

where I_{eo} refers to excitations from even to odd or vice versa, flipping the inversion eigenvalue, while I_{ee} corresponds to excitations from even to even or from odd to odd, and q_c denotes the component of $\mathbf{q}$ parallel to the trimer axis. These expressions can be motivated intuitively and also apply to the many-body case. An excitation from an even-parity bonding orbital to an odd-parity non-bonding state has vanishing matrix elements on the central site. The RIXS process has to be summed over the two outer sites with distance $2d$. Together with the flip of parity, this results in $\sin^2(q_c(2d)/2)$ behavior. Similarly, the $|\beta|^2 \cos^2(q_c d)$ term in I_{ee} arises from the two

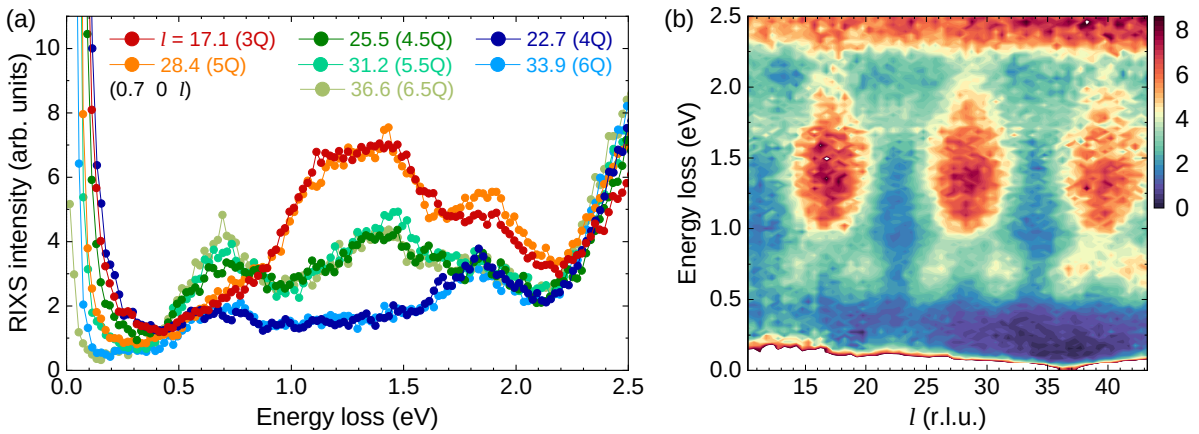

Fig. 11: Quasimolecular intra-t_{2g} excitations of the two-hole trimer $Ba_4NbIr_3O_{12}$ [93]. *a) RIXS spectra at selected* $\mathbf{q}$ *points, measured at 300 K at the Ir* L_3 *edge with 63 meV resolution. The overall behavior is equivalent to the case of Ir dimers, see Fig. 7: Peak intensities depend on* q_c *(along the trimer axis, parallel to the* c *axis) but peak energies do not. The elastic line is weak for* $q_c = 36.6 \cdot 2\pi/c$ *where the scattering angle is close to 90° but increases with decreasing* q_c*, i.e., decreasing* l*. b) RIXS intensity as a function of* q_c *and energy loss. The data show a modulation period of* $2\pi/(2d) \approx 5.67 \cdot 2\pi/c$ *around 0.7 eV and* $2\pi/d$ *around 1.5 eV. This reflects the Ir-Ir distances* d *and* $2d$ *and demonstrates the quasimolecular character.*

outer sites, now contributing with the same phase. The $|\delta|^2$ term stems from the scattering at the central site, for which the matrix elements may differ in size compared to the outer sites. Finally, the term proportional to $\gamma = (\beta^* \delta + \delta^* \beta)$ highlights the interference between scattering events at the central and outer trimer sites. Through the prefactors α, β, γ, and δ, the RIXS intensity provides a wealth of information about the quasimolecular wavefunction, see Fig. 10a).

Figure 11a) shows Ir L_3-edge RIXS spectra of $Ba_4NbIr_3O_{12}$ [93]. Equivalent to the dimer case, the RIXS spectra are rich and the peak intensities depend on q_c while the peak energies do not, pointing to a quasimolecular character. This is confirmed by the $\mathbf{q}$-dependent RIXS intensity, see Fig. 11b). A linear trimer exhibits two intra-trimer Ir-Ir distances, d and $2d$. The existence of two modulation periods $2\pi/d$ and $2\pi/(2d)$, see Eq. (11), is thus the hallmark signature of a quasimolecular electronic structure. In $Ba_4NbIr_3O_{12}$, the fast modulation of $I_{eo} \propto \sin^2(q_c d)$ with period π/d is observed around 0.7 eV, while the features above 1 eV roughly show $\sin^2(q_c d/2)$ behavior with a period of $2\pi/d$. The latter arises for $\gamma \ll -|\beta|^2$, see Eq. (11). This implies a dominant interference between central and outer sites, requiring a large weight of the wavefunction on the central site and opposite phases on the central site compared to the outer sites. The analysis roughly yields one hole on the central site and half a hole per outer site [93].

The rich physics of trimers offers an excellent opportunity to study the competition of spin-orbit coupling and hopping. Remarkably, a non-interacting picture that combines strong ζ with large hopping provides an intuitive explanation of the RIXS data. At the same time, the key RIXS features strongly restrict the relevant parameter range. Large $\zeta = 0.4$–0.5 eV is well established in iridates. From this starting point, the absence of RIXS features below 0.4 eV requires large hopping, see Fig. 10a). The RIXS intensity at low energy, around 0.7 eV, shows $\sin^2(q_c d)$ mod-

ulation, implying the excitation to an odd-parity non-bonding state. This requires that hopping does not exceed about 0.8 eV, see Fig. 10b). In this range, a dominant $\sin^2(q_c d)$ response at low energy is possible as the RIXS intensity of the excitation to the lowest (even) bonding $j = 3/2$ orbital nearly vanishes, see bottom right panel of Fig. 10a). Finally, the strong $\sin^2(q_c d/2)$ modulation above 1 eV mainly comes from excitations to antibonding $j = 1/2$ states.

In a non-interacting scenario, the ground state hosts two holes in the bonding j = 1/2 orbital, causing non-magnetic behavior. For finite hopping, the labeling as $j = 1/2$ or $3/2$ states is not fully correct since hopping is not diagonal in the j states for $t_{e_g^\pi}/t_{a_{1g}} \neq -1$. Hopping splits the local $j = 3/2$ quadruplets into two bonding doublets, a non-bonding quartet, and two antibonding doublets, see Fig. 10a). The splitting into doublets is caused by a finite mixing of $j = 1/2$ and $3/2$ character. Due to this mixing, the energy of the bonding $j = 1/2$ state is not perfectly linear in hopping. However, the deviations are small so that a discussion in terms of j states is still meaningful. This remains valid even upon considering electronic interactions with $U = 1.2$ eV and $J_H \approx 0.3$ eV, see Fig. 10b). Coulomb interactions slightly affect the excitation energies and lift degeneracies of multiplets. However, this has only a minor effect on the two-hole ground state and the overall behavior. On the trimer, large hopping wins against correlations. This in particular applies to $Ba_4NbIr_3O_{12}$ with fewer holes than Ir sites. The main conclusion is very similar to the case of face-sharing Ir dimers: The two-hole trimer compound $Ba_4NbIr_3O_{12}$ exhibits a quasimolecular electronic structure that, to a large extent, can be understood in a non-interacting picture. Both large spin-orbit coupling and large hopping are decisive. In the ground state, two holes occupy a spin-orbit-entangled bonding $j = 1/2$ orbital.

5.3 Between Mott and cluster Mott: face-sharing $4d$ Ru dimers

Face-sharing $4d^4$ Ru dimers form a non-trivial bridge between d^4 Mott insulators such as K_2OsCl_6 (Sec. 4.1) and the cluster Mott behavior found in $5d$ Ir dimers (Sec. 5.2). In the latter, large hopping yields quasimolecular behavior, but $4d$ ruthenates realize a different part of phase space. The $4d^4$ dimer $Ba_3CeRu_2O_9$ is located in the intricate but hardly explored crossover regime *between* the Mott limit and the quasimolecular limit [94]. Like the iridate sister compounds, the ruthenates $Ba_3MRu_2O_9$ exist for M ions with different valences [122–124]. Using Ru L_3-edge RIXS for $M = Ce^{4+}$ with four-hole Ru dimers [94], we find that the electronic structure is governed by a delicate balance of competing interactions. Hopping, Hund's coupling, and trigonal crystal-field splitting Δ_{trig} are of comparable size, giving rise to a rich phase diagram [28, 94, 98]. Spin-orbit coupling $\zeta = 0.15$ eV is the smallest electronic parameter but decisive for the spin-orbit-entangled singlet character of the ground state.

The $4d$ Ru L_3 edge is at about 2.84 keV in the tender x-ray range, a challenging regime. RIXS with a resolution of ≈ 60 meV can be measured at PETRA III [24]. Compared to the Ir L edge, the smaller incident energy restricts the range of $\mathbf{q}$ that can be studied. Figure 12a) shows RIXS spectra for fixed modulus $|\mathbf{q}|$, measured over a wide range of angle of incidence θ. Compared to the d^4 Mott limit, see Fig. 3, the data are very rich. The competition of hopping, J_H, Δ_{trig}, and ζ produces a large number of excitations, preventing a simple peak assignment [94].

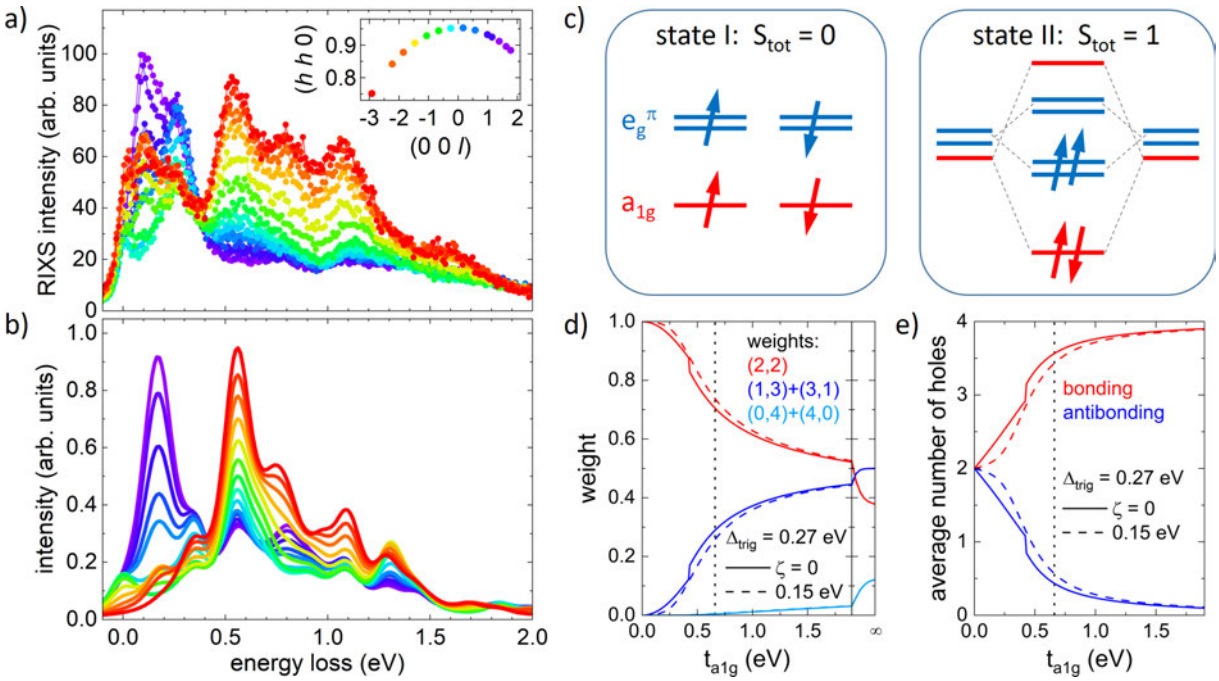

Fig. 12: Between Mott and cluster Mott: the $4d^4$ dimer $Ba_3CeRu_2O_9$ [94]. *a) Ru L_3-edge RIXS spectra measured at 20 K for different angles of incidence. Inset: corresponding* $\mathbf{q}$ *points. b) Numerical results for $U = 2$ eV, $J_H = 0.26$ eV, $\zeta = 0.15$ eV, $\Delta_{trig} = 0.27$ eV, $t_{a_{1g}} = 0.66$ eV, and $t_{e_g^\pi}/t_{a_{1g}} = -0.45$. c) Sketches of the electronic structure in the Mott limit and the quasimolecular limit for $\Delta_{trig} > 0$ and $\zeta = 0$. d) Cumulative weights w_{nm} for n holes on one site in the ground state as a function of $t_{a_{1g}}$ for fixed $t_{e_g^\pi}/t_{a_{1g}} = -0.45$. Vertical dotted line highlights $t_{a_{1g}} = 0.66$ eV. e) Average number of holes in bonding and antibonding orbitals in the ground state.*

The RIXS intensity of all peaks strongly varies with θ. The angle of incidence sets $\mathbf{q}$ as well as the polarization. Unfortunately, it is not trivial to disentangle the $\mathbf{q}$-dependent interference pattern from polarization effects. As discussed above, the RIXS intensity is the squared sum of several terms, where each term carries its own dependence on $\mathbf{q}$ and polarization. For hard x-ray RIXS on $5d$ compounds, covering several periods of the interference pattern, the polarization determines the envelope (see, e.g., Fig. 9d)). At the Ru L_3 edge, however, RIXS can explore only about one period in $Ba_3CeRu_2O_9$. In this case, a discussion of the modulation requires a careful analysis [94], which we skip here for simplicity.

We determine the electronic parameters by numerical simulation of the RIXS spectra, see Fig. 12b). Best agreement is found for $U = 2$ eV, $J_H = 0.26$ eV, $\zeta = 0.15$ eV, $\Delta_{\text{trig}} = 0.27$ eV, $t_{a_{1g}} = 0.66$ eV, and $t_{e_g^\pi}/t_{a_{1g}} = -0.45$. The values for U, J_H, and ζ are well within the expected range for ruthenates, while Δ_{trig} and the hoppings are more material-specific parameters. The numerical results reproduce the key features of the RIXS data, describing the overall peak structure and the pronounced dependence on θ. For small θ, i.e., positive l (purple), the intensity is maximized below about 0.4 eV but suppressed above 0.4 eV.

To understand the puzzling ground state, we first discuss the limiting cases of small and large hopping, considering $\zeta = 0$ for simplicity. In the Mott limit, the on-site Coulomb repulsion U suppresses charge fluctuations. Each Ru site hosts two holes that form spin $S = 1$ due to

Hund's coupling (cubic $^3T_1$ multiplet, see Tab. 1). For positive Δ_{trig}, there is one hole in the a_{1g} orbital and one in an e_g^π orbital, see state I in Fig. 12c). Hopping is diagonal in the a_{1g}-e_g^π basis and yields exchange interactions. The degenerate e_g^π orbitals exhibit a Kugel-Khomskii-type exchange, favoring parallel spins on the two sites. Nevertheless, the ground state shows S_{tot}=0 since the larger antiferromagnetic coupling driven by $t_{a_{1g}}$ wins. In the opposite quasimolecular limit of large hopping, the lowest bonding orbital has a_{1g} character since $|t_{a_{1g}}| > |t_{e_g^\pi}|$, see state II in Fig. 12c). This yields two holes in the bonding a_{1g} orbital and two holes within the four bonding e_g^π states. The two e_g^π holes form a triplet with $S_{\text{tot}} = 1$ due to Hund's coupling.

The intermediate regime, between Mott and cluster Mott, needs a more quantitative discussion. Concerning the character of the ground state, we consider the cumulative weights w_{nm} of terms showing n holes on one site and $m = 4-n$ on the other, see Fig. 12d). The Mott limit is characterized by $w_{22} \approx 1$, i.e., roughly two holes per site. With increasing hopping, the weight of states with $n \neq 2$ increases. The quasimolecular limit, reached for infinite hopping, exhibits $w_{22} = 3/8$ and $w_{13}+w_{31} = 1/2$. For the parameters appropriate for $Ba_3CeRu_2O_9$, the weights w_{nm} are plotted in Fig. 12d) as a function of $t_{a_{1g}}$, both for $\zeta = 0$ (solid) and $0.15\,$eV (dashed). For $\zeta = 0$, the jump of w_{22} close to $t_{a_{1g}} = 0.4\,$eV marks the phase transition between the more localized state I with S_{tot}=0 and state II with S_{tot}=1. In the discussion above, state II has been motivated from a quasimolecular perspective, while state I follows naturally for the Mott limit. We emphasize that state II violates Hund's rule (not showing S=1 per site) and cannot be motivated by exchange coupling between d^4 sites. Nevertheless, state II is already realized for moderate $t_{a_{1g}} \approx 0.4\,$eV, where $w_{22} > 0.8$ still indicates a localized character. With $t_{a_{1g}} = 0.66\,$eV (vertical dotted line), $Ba_3CeRu_2O_9$ falls within the regime of state II, but the degree of Mott localization is still sizable. We find $w_{22} = 0.70\ (0.74)$ for $\zeta, = 0\ (0.15)\,$eV. These values are within the intermediate regime but closer to the Mott limit, $w_{22} = 1$, than to the quasimolecular limit, $w_{22} = 3/8$.

The intermediate character of $Ba_3CeRu_2O_9$ is supported by the average number of holes in bonding and antibonding states, n_{B} and n_{AB}, see Fig. 12e). In the quasimolecular limit, all four holes occupy bonding orbitals, $n_{\text{B}} = 4$. In the Mott limit, the four holes are distributed equally over the (anti-)bonding orbitals, $n_{\text{B}} = n_{\text{AB}} = 2$. For the parameters of $Ba_3CeRu_2O_9$, the phase transition between states I and II occurs around $t_{a_{1g}} = 0.4\,$eV where $n_{\text{B}} \approx 3$, halfway between the two limits. For $t_{a_{1g}} = 0.66\,$eV, we find $n_{\text{B}} = 3.6\ (3.4)$ for $\zeta = 0\ (0.15)\,$eV. This provides a quantitative measure of the intermediate character of $Ba_3CeRu_2O_9$. With $w_{22} \gtrsim 0.70$, the charge distribution tends to the Mott limit with predominantly two holes per Ru site, minimizing the Coulomb energy. At the same time, the average number of holes in bonding orbitals is large, $n_{\text{B}} \gtrsim 3.4$, pointing to the quasimolecular limit. In the $4d^4$ ruthenate dimer compound $Ba_3CeRu_2O_9$, the dichotomy between localized states in the Mott limit and quasimolecular states in the cluster Mott case breaks down.

In $4d$ ruthenates, compared to iridates, the smaller hopping boosts the role of correlations for the cluster moments. The physics of the intermediate regime has hardly been explored. For $4d^4$ Ru dimers, the vivid competition of Hund's coupling, hopping, and crystal field yields a

series of distinct ground states (for $\zeta = 0$) [94].[13] Hopping and crystal field can be tuned by, e.g., external pressure, potentially allowing for control of the local physics. Spin-orbit coupling turns the phase transitions into crossovers, but the electronic structure and the low-energy excitations are still highly sensitive to a change of the electronic parameters. In $Ba_3MRu_2O_9$ with M^{3+} ions and five holes per dimer, such a strong sensitivity has been reported [125].

Acknowledgement

It is a pleasure to acknowledge the (former) PhD students most closely involved in this project: A. Revelli, M. Magnaterra, P. Warzanowski, L. Pätzold, E. Bergamasco, J. Attig, and A. Sandberg. The results discussed here are based on several fruitful collaborations. We would like to recognize the long-standing members of our team: M. Moretti Sala, G. Monaco, P. van Loosdrecht, H. Gretarsson, and C. Sahle on the experimental side and M. Hermanns, S. Trebst, and J. van den Brink on the theory side. All of the experimental data shown here were measured on single crystals provided by the group of P. Becker and L. Bohatý. We acknowledge the European Synchrotron Radiation Facility (ESRF) for providing beam time at beamline ID20. We acknowledge DESY – a member of the Helmholtz Association HGF – for access to beam time. Furthermore, we acknowledge funding from the Deutsche Forschungsgemeinschaft (DFG, German Research Foundation) through Project No. 277146847 – CRC 1238 (project B03).

[13] For $Ba_3CeRu_2O_9$, we focused on $\Delta_{\text{trig}} > 0$, but more states can be realized if we skip this restriction [94].

References

[1] L.J.P. Ament, M. van Veenendaal, T.P. Devereaux, J.P. Hill, and J. van den Brink, Rev. Mod. Phys. **83**, 705 (2011)

[2] T. Tohyama, J. Electron Spectrosc. Relat. Phenom. **200**, 209 (2015)

[3] M. Mitrano, S. Johnston, Y.-J. Kim, and M. Dean, Phys. Rev. X **14**, 040501 (2024)

[4] F.M. de Groot, M.W. Haverkort, H. Elnaggar, A. Juhin, K.-J. Zhou, and P. Glatzel, Nat. Rev. Methods Primers **4**, 45 (2024)

[5] F. Gel'mukhanov, M. Odelius, S.P. Polyutov, A. Föhlisch, and V. Kimberg, Rev. Mod. Phys. **93**, 035001 (2021)

[6] J. van den Brink: *Resonant Inelastic X-ray Scattering on Elementary Excitations*, in E. Pavarini, E. Koch, J. van den Brink, and G. Sawatzky (Eds.): *Quantum Materials: Experiments and Theory*, Modeling and Simulation, Vol. 6 (FZ Jülich, 2016) `http://www.cond-mat.de/events/correl16`

[7] L. Braicovich, J. van den Brink, V. Bisogni, M. Moretti Sala, L.J.P. Ament, N.B. Brookes, G.M. De Luca, M. Salluzzo, T. Schmitt, V.N. Strocov, and G. Ghiringhelli, Phys. Rev. Lett. **104**, 077002 (2010)

[8] J. Kim, D. Casa, M.H. Upton, T. Gog, Y.-J. Kim, J.F. Mitchell, M. van Veenendaal, M. Daghofer, J. van den Brink, G. Khaliullin, and B.J. Kim, Phys. Rev. Lett. **108**, 177003 (2012)

[9] J. Kim, A.H. Said, D. Casa, M.H. Upton, T. Gog, M. Daghofer, G. Jackeli, J. van den Brink, G. Khaliullin, and B.J. Kim, Phys. Rev. Lett. **109**, 157402 (2012)

[10] J. Kim, M. Daghofer, A.H. Said, T. Gog, J. van den Brink, G. Khaliullin, and B.J. Kim, Nat. Commun. **5**, 4453 (2014)

[11] M. Le Tacon, G. Ghiringhelli, J. Chaloupka, M. Moretti Sala, V. Hinkov, M.W. Haverkort, M. Minola, M. Bakr, K.J. Zhou, S. Blanco-Canosa, C. Monney, Y.T. Song, G.L. Sun, C.T. Lin, G.M. De Luca, M. Salluzzo, G. Khaliullin, T. Schmitt, L. Braicovich, and B. Keimer, Nat. Phys. **7**, 725 (2011)

[12] J. Schlappa, K. Wohlfeld, K.J. Zhou, M. Mourigal, M.W. Haverkort, V.N. Strocov, L. Hozoi, C. Monney, S. Nishimoto, S. Singh, A. Revcolevschi, J.-S. Caux, L. Patthey, H.M. Rønnow, J. van den Brink, and T. Schmitt, Nature **485**, 82 (2012)

[13] Y. Tseng, E. Paris, K.P. Schmidt, W. Zhang, T.C. Asmara, R. Bag, V.N. Strocov, S. Singh, J. Schlappa, H.M. Rønnow, and T. Schmitt, Commun. Phys. **6**, 138 (2023)

[14] V. Bisogni, L. Simonelli, L.J.P. Ament, F. Forte, M. Moretti Sala, M. Minola, S. Huotari, J. van den Brink, G. Ghiringhelli, N.B. Brookes, and L. Braicovich, Phys. Rev. B **85**, 214527 (2012)

[15] M. Rossi, P. Marabotti, Y. Hirata, G. Monaco, M. Krisch, K. Ohgushi, K. Wohlfeld, J. van den Brink, and M. Moretti Sala, Eur. Phys. J. Plus **135**, 676 (2020)

[16] J. Schlappa, U. Kumar, K.J. Zhou, S. Singh, M. Mourigal, V.N. Strocov, A. Revcolevschi, L. Patthey, H.M. Rønnow, S. Johnston, and T. Schmitt, Nat. Commun. **9**, 5394 (2018)

[17] J. Schlappa, T. Schmitt, F. Vernay, V.N. Strocov, V. Ilakovac, B. Thielemann, H.M. Rønnow, S. Vanishri, A. Piazzalunga, X. Wang, L. Braicovich, G. Ghiringhelli, C. Marin, J. Mesot, B. Delley, and L. Patthey, Phys. Rev. Lett. **103**, 047401 (2009)

[18] J. Li, Y. Gu, Y. Takahashi, K. Higashi, T. Kim, Y. Cheng, F. Yang, J. Kuneš, J. Pelliciari, A. Hariki, and V. Bisogni, Phys. Rev. X **13**, 011012 (2023)

[19] H. Elnaggar, A. Nag, M.W. Haverkort, M. Garcia-Fernandez, A. Walters, R.-P. Wang, K.-J. Zhou, and F. de Groot, Nat. Commun. **14**, 2749 (2023)

[20] M. Magnaterra, K. Hopfer, Ch.J. Sahle, M. Moretti Sala, G. Monaco, J. Attig, C. Hickey, I.-M. Pietsch, F. Breitner, P. Gegenwart, M.H. Upton, Jungho Kim, S. Trebst, P.H.M. van Loosdrecht, J. van den Brink, and M. Grüninger, arXiv:2301.08340 (2023)

[21] N.B. Brookes, F. Yakhou-Harris, K. Kummer, A. Fondacaro, J.C. Cezar, D. Betto, E. Velez-Fort, A. Amorese, G. Ghiringhelli, L. Braicovich, R. Barrett, G. Berruyer, F. Cianciosi, L. Eybert, P. Marion, P. van der Linden, and L. Zhang, Nucl. Instrum. Meth. A **903**, 175 (2018)

[22] M. Moretti Sala, C. Henriquet, L. Simonelli, R. Verbeni, and G. Monaco, J. Electron Spectrosc. Relat. Phenom. **188**, 150 (2013)

[23] M. Moretti Sala, K. Martel, C. Henriquet, A. Al Zein, L. Simonelli, C.J. Sahle, H. Gonzalez, M.-C. Lagier, C. Ponchut, S. Huotari, R. Verbeni, M. Krisch, and G. Monaco, J. Synchrotron Rad. **25**, 580 (2018)

[24] H. Gretarsson, D. Ketenoglu, M. Harder, S. Mayer, F.-U. Dill, M. Spiwek, H. Schulte-Schrepping, M. Tischer, H.-C. Wille, B. Keimer, and H. Yavaş, J. Synchrotron Rad. **27**, 538 (2020)

[25] L.J.P. Ament, G. Khaliullin, and J. van den Brink, Phys. Rev. B **84**, 020403(R) (2011)

[26] K. Ishii, I. Jarrige, M. Yoshida, K. Ikeuchi, J. Mizuki, K. Ohashi, T. Takayama, J. Matsuno, and H. Takagi, Phys. Rev. B **83**, 115121 (2011)

[27] J. Kim, D. Casa, A. Said, R. Krakora, B.J. Kim, E. Kasman, X. Huang, and T. Gog, Sci. Rep. **8**, 1958 (2018)

[28] D.I. Khomskii and S.V. Streltsov, Chem. Rev. **121**, 2992 (2021)

[29] E. Benckiser, L. Fels, G. Ghiringhelli, M. Moretti Sala, T. Schmitt, J. Schlappa, V.N. Strocov, N. Mufti, G.R. Blake, A.A. Nugroho, T.T.M. Palstra, M.W. Haverkort, K. Wohlfeld, and M. Grüninger, Phys. Rev. B **88**, 205115 (2013)

[30] W. Schülke: *Electron Dynamics by Inelastic X-Ray Scattering* (Oxford University Press, New York, 2007)

[31] M. Krisch and F. Sette: *Inelastic X-Ray Scattering from Phonons*, in M. Cardona, R. Merlin (Eds.): *Light Scattering in Solids IX. Topics in Applied Physics **108*** (Springer, Berlin, Heidelberg, 2006)

[32] M. Mohr, J. Maultzsch, E. Dobardžić, S. Reich, I. Milošević, M. Damnjanović, A. Bosak, M. Krisch, and C. Thomsen, Phys. Rev. B **76**, 035439 (2007)

[33] L.H. Tjeng: *Imaging Orbitals with X-rays*, in E. Pavarini and E. Koch (Eds.): *Orbital Physics in Correlated Matter*, Modeling and Simulation, Vol. 13 (FZ Jülich, 2023) `http://www.cond-mat.de/events/correl23`

[34] Y. Shvyd'ko, S. Stoupin, D. Shu, S.P. Collins, K. Mundboth, J. Sutter, and M. Tolkiehn, Nat. Commun. **5**, 4219 (2014)

[35] M.W. Haverkort, Phys. Rev. Lett. **105**, 167404 (2010)

[36] P. Warzanowski, M. Magnaterra, Ch.J. Sahle, M. Moretti Sala, P. Becker, L. Bohatý, I. Císařová, G. Monaco, T. Lorenz, P.H.M. van Loosdrecht, J. van den Brink, and M. Grüninger, Phys. Rev. B **110**, 195120 (2024)

[37] S.G. Chiuzbăian, G. Ghiringhelli, C. Dallera, M. Grioni, P. Amann, X. Wang, L. Braicovich, and L. Patthey, Phys. Rev. Lett. **95**, 197402 (2005)

[38] G. Ghiringhelli, M. Matsubara, C. Dallera, F. Fracassi, R. Gusmeroli, A. Piazzalunga, A. Tagliaferri, N.B. Brookes, A. Kotani, and L. Braicovich, J. Phys.: Condens. Matter **17**, 5397 (2005)

[39] S. Huotari, T. Pylkkänen, G. Vankó, R. Verbeni, P. Glatzel, and G. Monaco, Phys. Rev. B **78**, 041102(R) (2008)

[40] L.-C. Duda, T. Schmitt, M. Magnuson, J. Forsberg, A. Olsson, J. Nordgren, K. Okada, and A. Kotani, Phys. Rev. Lett. **96**, 067402 (2006)

[41] C.-Y. Liu, K. Ruotsalainen, K. Bauer, R. Decker, A. Pietzsch, and A. Föhlisch, Phys. Rev. B **106**, 035104 (2022)

[42] G. Ghiringhelli, A. Piazzalunga, C. Dallera, T. Schmitt, V.N. Strocov, J. Schlappa, L. Patthey, X. Wang, H. Berger, and M. Grioni, Phys. Rev. Lett. **102**, 027401 (2009)

[43] D. Betto, Y.Y. Peng, S.B. Porter, G. Berti, A. Calloni, G. Ghiringhelli, and N.B. Brookes, Phys. Rev. B **96**, 020409(R) (2017)

[44] A. Nag, H.C. Robarts, F. Wenzel, J. Li, H. Elnaggar, R.-P. Wang, A.C. Walters, M. García-Fernández, F.M.F. de Groot, M.W. Haverkort, and K.-J. Zhou, Phys. Rev. Lett. **124**, 067202 (2020)

[45] P. Warzanowski, M. Magnaterra, P. Stein, G. Schlicht, Q. Faure, Ch.J. Sahle, T. Lorenz, P. Becker, L. Bohatý, M. Moretti Sala, G. Monaco, P.H.M. van Loosdrecht, and M. Grüninger, Phys. Rev. B **108**, 125120 (2023)

[46] S. Sugano, Y. Tanabe, and H. Kamimura: *Multiplets of Transition-Metal Ions in Crystals* (Academic Press, New York, 1970)

[47] A. Georges, L. de'Medici, and J. Mravlje, Ann. Rev. Condens. Matter Phys. **4**, 137 (2013)

[48] G. Zhang and E. Pavarini, Phys. Rev. B **95**, 075145 (2017)

[49] P. Warzanowski, M. Magnaterra, G. Schlicht, Q. Faure, Ch.J. Sahle, P. Becker, L. Bohatý, M. Moretti Sala, G. Monaco, M. Hermanns, P.H.M. van Loosdrecht, and M. Grüninger, Phys. Rev. B **109**, 155149 (2024)

[50] W. Witczak-Krempa, G. Chen, Y.B. Kim, and L. Balents, Annu. Rev. Condens. Matter Phys. **5**, 57 (2014)

[51] J.G. Rau, E.K.-H. Lee, and H.-Y. Kee, Annu. Rev. Condens. Matter Phys. **7**, 195 (2016)

[52] R. Schaffer, E.K.-H. Lee, B.-J. Yang, and Y.B. Kim, Rep. Prog. Phys. **79**, 094504 (2016)

[53] S.V. Streltsov and D.I. Khomskii, Phys. Rev. X **10**, 031043 (2020)

[54] T. Takayama, J. Chaloupka, A. Smerald, G. Khaliullin, and H. Takagi, J. Phys. Soc. Jpn. **90**, 062001 (2021)

[55] L.V. Pourovskii, D. Fiore Mosca, L. Celiberti, S. Khmelevskyi, A. Paramekanti, and C. Franchini, Nat. Rev. Mater. **10**, 674 (2025)

[56] G. Khaliullin, Phys. Rev. Lett. **111**, 197201 (2013)

[57] G. Jackeli and G. Khaliullin, Phys. Rev. Lett. **102**, 017205 (2009)

[58] S.H. Chun, J.-W. Kim, J. Kim, H. Zheng, C.C. Stoumpos, C.D. Malliakas, J.F. Mitchell, K. Mehlawat, Y. Singh, Y. Choi, T. Gog, A. Al-Zein, M. Moretti Sala, M. Krisch, J. Chaloupka, G. Jackeli, G. Khaliullin, and B.J. Kim, Nat. Phys. **11**, 462 (2015)

[59] Q. Wang, A. de la Torre, J.A. Rodriguez-Rivera, A.A. Podlesnyak, W. Tian, A- A. Aczel, M. Matsuda, P.J. Ryan, J.-W. Kim, J.G. Rau, and K.W. Plumb, Phys. Rev. X **15**, 021021 (2025)

[60] N. Iwahara and W. Furukawa, Phys. Rev. B **108**, 075136 (2023)

[61] J.E. Fergusson and P.F. Heveldt, Aust. J. Chem. **27**, 661 (1974)

[62] R.L. Armstrong, D. Mintz, B.M. Powell, and W.J.L. Buyers, Phys. Rev. B **17**, 1260 (1978)

[63] M. Saura-Múzquiz, M. Avdeev, H.E.A. Brand, and B.J. Kennedy, Inorg. Chem. **61**, 15961 (2022)

[64] D.I. Khomskii: *Transition metal compounds* (Cambridge University Press, 2014)

[65] A. Jain, M. Krautloher, J. Porras, G. H. Ryu, D. P. Chen, D. L. Abernathy, J. T. Park, A. Ivanov, J. Chaloupka, G. Khaliullin, B. Keimer, and B.J. Kim, Nat. Phys. **13**, 633 (2017)

[66] S. Kunkemöller, D. Khomskii, P. Steffens, A. Piovano, A.A. Nugroho, and M. Braden, Phys. Rev. Lett. **115**, 247201 (2015)

[67] H. Gretarsson, H. Suzuki, Hoon Kim, K. Ueda, M. Krautloher, B.J. Kim, H. Yavaş, G. Khaliullin, and B. Keimer, Phys. Rev. B **100**, 045123 (2019)

[68] G. Zhang and E. Pavarini, Phys. Rev. B **101**, 205128 (2020)

[69] T. Feldmaier, P. Strobel, M. Schmid, P. Hansmann, and M. Daghofer, Phys. Rev. Res. **2**, 033201 (2020)

[70] I. Vergara, M. Magnaterra, P. Warzanowski, J. Attig, S. Kunkemöller, D.I. Khomskii, M. Braden, M. Hermanns, and M. Grüninger, Phys. Rev. B **106**, 085103 (2022)

[71] B.J. Kim and G. Khaliullin, Phys. Rev. B **96**, 085108 (2017)

[72] N. Iwahara and S. Shikano, Phys. Rev. Res. **5**, 023051 (2023)

[73] B. Yuan, J.P. Clancy, A.M. Cook, C.M. Thompson, J. Greedan, G. Cao, B.C. Jeon, T.W. Noh, M.H. Upton, D. Casa, T. Gog, A. Paramekanti, and Y.-J. Kim, Phys. Rev. B **95**, 235114 (2017)

[74] M. Kusch, V.M. Katukuri, N.A. Bogdanov, B. Büchner, T. Dey, D.V. Efremov, J.E. Hamann-Borrero, B.H. Kim, M. Krisch, A. Maljuk, M. Moretti Sala, S. Wurmehl, G. Aslan-Cansever, M. Sturza, L. Hozoi, J. van den Brink, and J. Geck, Phys. Rev. B **97**, 064421 (2018)

[75] A. Nag, S. Bhowal, A. Chakraborty, M.M. Sala, A. Efimenko, F. Bert, P.K. Biswas, A.D. Hillier, M. Itoh, S.D. Kaushik, V. Siruguri, C. Meneghini, I. Dasgupta, and S. Ray, Phys. Rev. B **98**, 014431 (2018)

[76] A.A. Aczel, Q. Chen, J.P. Clancy, C. dela Cruz, D. Reig-i-Plessis, G.J. MacDougall, C.J. Pollock, M.H. Upton, T.J. Williams, N. LaManna, J.P. Carlo, J. Beare, G.M. Luke, and H.D. Zhou, Phys. Rev. Mater. **6**, 094409 (2022)

[77] S. Calder, D.J. Singh, V.O. Garlea, M.D. Lumsden, Y.G. Shi, K. Yamaura, and A.D. Christianson, Phys. Rev. B **96**, 184426 (2017)

[78] E. Kermarrec, C.A. Marjerrison, C.M. Thompson, D.D. Maharaj, K. Levin, S. Kroeker, G.E. Granroth, R. Flacau, Z. Yamani, J.E. Greedan, and B.D. Gaulin, Phys. Rev. B **91**, 075133 (2015)

[79] S. Calder, J.G. Vale, N.A. Bogdanov, X. Liu, C. Donnerer, M.H. Upton, D. Casa, A.H. Said, M.D. Lumsden, Z. Zhao, J.-Q. Yan, D. Mandrus, S. Nishimoto, J. van den Brink, J.P. Hill, D.F. McMorrow, and A.D. Christianson, Nat. Commun. **7**, 11651 (2016)

[80] A.E. Taylor, R. Morrow, R.S. Fishman, S. Calder, A.I. Kolesnikov, M.D. Lumsden, P.M. Woodward, and A.D. Christianson, Phys. Rev. B **93**, 220408(R) (2016)

[81] A.E. Taylor, R. Morrow, M.D. Lumsden, S. Calder, M.H. Upton, A.I. Kolesnikov, M.B. Stone, R.S. Fishman, A. Paramekanti, P.M. Woodward, and A.D. Christianson, Phys. Rev. B **98**, 214422 (2018)

[82] A.E. Taylor, S. Calder, R. Morrow, H.L. Feng, M.H. Upton, M.D. Lumsden, K. Yamaura, P.M. Woodward, and A.D. Christianson, Phys. Rev. Lett. **118**, 207202 (2017)

[83] B. Henderson and G.F. Imbusch: *Optical spectroscopy of inorganic solids* (Oxford, 1989)

[84] B.N. Figgis and M.A. Hitchman: *Ligand Field Theory and its Applications* (Wiley, 1999)

[85] P.E. Hoggard, Z. Naturforsch. **36a**, 1276 (1981)

[86] H. Kamimura, S. Koide, H. Sekiyama, and S. Sugano, J. Phys. Soc. Jpn. **15**, 1264 (1960)

[87] A. Bertin, T. Dey, D. Brüning, D. Gorkov, K. Jenni, A. Krause, P. Becker, L. Bohatý, D. Khomskii, V. Pomjakushin, L. Keller, M. Braden, and T. Lorenz, Phys. Rev. B **109**, 094409 (2024)

[88] M.W. Haverkort, M. Zwierzcki, and O.K. Andersen, Phys. Rev. B **85**, 165113 (2012)

[89] M.W. Haverkort, J. Phys.: Conf. Ser. **712**, 012001 (2016)

[90] A. Revelli, M. Moretti Sala, G. Monaco, P. Becker, L. Bohatý, M. Hermanns, T.C. Koethe, T. Fröhlich, P. Warzanowski, T. Lorenz, S. V. Streltsov, P.H.M. van Loosdrecht, D.I. Khomskii, J. van den Brink, and M. Grüninger, Sci. Adv. **5**, eaav4020 (2019)

[91] A. Revelli, M. Moretti Sala, G. Monaco, M. Magnaterra, J. Attig, L. Peterlini, T. Dey, A.A. Tsirlin, P. Gegenwart, T. Fröhlich, M. Braden, C. Grams, J. Hemberger, P. Becker, P.H.M. van Loosdrecht, D.I. Khomskii, J. van den Brink, M. Hermanns, and M. Grüninger, Phys. Rev. B **106**, 155107 (2022)

[92] M. Magnaterra, J. Attig, L. Peterlini, M. Hermanns, M.H. Upton, J. Kim, L. Prodan, V. Tsurkan, I. Kézsmárki, P.H.M. van Loosdrecht, and M. Grüninger, Phys. Rev. Lett. **133**, 046501 (2024)

[93] M. Magnaterra, A. Sandberg, H. Schilling, P. Warzanowski, L. Pätzold, E. Bergamasco, Ch.J. Sahle, B. Detlefs, K. Ruotsalainen, M. Moretti Sala, G. Monaco, P. Becker, Q. Faure, G.S. Thakur, M. Songvilay, C. Felser, P.H.M. van Loosdrecht, J. van den Brink, M. Hermanns, and M. Grüninger, Phys. Rev. B **111**, 085122 (2025)

[94] L. Pätzold, A. Sandberg, H. Schilling, H. Gretarsson, E. Bergamasco, M. Magnaterra, P. Becker, P.H.M. van Loosdrecht, J. van den Brink, M. Hermanns, and M. Grüninger, npj Quantum Mater. **11**, 48 (2026)

[95] M. Magnaterra, M. Moretti Sala, G. Monaco, P. Becker, M. Hermanns, P. Warzanowski, T. Lorenz, D.I. Khomskii, P.H.M. van Loosdrecht, J. van den Brink, and M. Grüninger, Phys. Rev. Res. **5**, 01316 (2023)

[96] G.V. Chen and C. Wu, npj Quantum Mater. **9**, 1 (2024)

[97] V. Jayakumar and C. Hickey, Phys. Rev. B **113**, 035151 (2026)

[98] Y. Li, A.A. Tsirlin, T. Dey, P. Gegenwart, R. Valentí, and S.M. Winter, Phys. Rev. B **102**, 235142 (2020)

[99] Y. Ma and M. Blume, Rev. Sci. Instrum. **66**, 1543 (1995)

[100] F. Gel'mukhanov and H. Ågren, Phys. Rev. A **49**, 4378 (1994)

[101] V.M. Katukuri, X. Lu, D.E. McNally, M. Dantz, V.N. Strocov, M. Moretti Sala, M.H. Upton, J. Terzic, G. Cao, O.V. Yazyev, and T. Schmitt, Phys. Rev. B **105**, 075114 (2022)

[102] J. Söderström, A. Ghosh, L. Kjellsson, V. Ekholm, T. Tokushima, C. Såthe, N. Velasquez, M. Simon, O. Björneholm, L. Duda, A.N. de Brito, M. Odelius, J.-C. Liu, J. Wang, V. Kimberg, M. Agåker, J.-E. Rubensson, and F. Gel'mukhanov, Sci. Adv. **10**, eadk3114 (2024)

[103] V.K. Bhartiya, T. Kim, J. Li, T.P. Darlington, D.J. Rizzo, Y. Gu, S. Fan, C. Nelson, J.W. Freeland, X. Xu, D.N. Basov, J. Pelliciari, A.F. May, C. Mazzoli, and V. Bisogni, npj Quantum Mater. **10**, 80 (2025)

[104] T. Ren, Y. Shen, S.F.R. TenHuisen, J. Sears, W. He, M.H. Upton, D. Casa, P. Becker, M. Mitrano, M.P.M. Dean, and R.M. Konik, arXiv:2404.05850 (2024)

[105] J. Kwon, J. Kim, G. Oh, S. Jin, K. Kim, H. Kim, S. Ha, H.-W.J. Kim, G. Sim, B. Wehinger, G. Garbarino, N. Maraytta, M. Merz, M. Le Tacon, C.J. Sahle, A. Longo, J. Kim, A. Go, G.Y. Cho, B.H. Kim, and B.J. Kim, Nat. Mater. **25**, 610 (2026)

[106] M. Moretti Sala, V. Schnells, S. Boseggia, L. Simonelli, A. Al-Zein, J.G. Vale, L. Paolasini, E.C. Hunter, R.S. Perry, D. Prabhakaran, A.T. Boothroyd, M. Krisch, G. Monaco, H.M. Rønnow, D.F. McMorrow, and F. Mila, Phys. Rev. B **92**, 024405 (2015)

[107] Z. Porter, P.M. Sarte, T. Petersen, M.H. Upton, L. Hozoi, and S.D. Wilson, Phys. Rev. B **106**, 115140 (2022)

[108] L.T. Nguyen and R.J. Cava, Chem. Rev. **121**, 2935 (2021)

[109] T. Dey, M. Majumder, J.C. Orain, A. Senyshyn, M. Prinz-Zwick, S. Bachus, Y. Tokiwa, F. Bert, P. Khuntia, N. Büttgen, A.A. Tsirlin, and P. Gegenwart, Phys. Rev. B **96**, 174411 (2017)

[110] T. Sakamoto, Y. Doi, and Y. Hinatsu, J. Solid State Chem. **179**, 2595 (2006)

[111] T. Dey, A.V. Mahajan, P. Khuntia, M. Baenitz, B. Koteswararao, and F.C. Chou, Phys. Rev. B **86**, 140405(R) (2012)

[112] R. Kumar, D. Sheptyakov, P. Khuntia, K. Rolfs, P.G. Freeman, H.M. Rønnow, T. Dey, M. Baenitz, and A.V. Mahajan, Phys. Rev. B **94**, 174410 (2016)

[113] W.-J. Lee, S.-H. Do, Sungwon Yoon, S. Lee, Y.S. Choi, D.J. Jang, M. Brando, M. Lee, E.S. Choi, S. Ji, Z.H. Jang, B.J. Suh, and K.-Y. Choi, Phys. Rev. B **96**, 014432 (2017)

[114] H. Zhao, Y. Zhang, P. Schlottmann, R. Nandkishore, L.E. DeLong, and G. Cao, Phys. Rev. Lett. **132**, 226503 (2024)

[115] L.T. Nguyen and R.J. Cava, Phys. Rev. Mater. **3**, 014412 (2019)

[116] G.S. Thakur, S. Chattopadhyay, T. Doert, T. Herrmannsdörfer, and C. Felser, Cryst. Growth Des. **20**, 2871 (2020)

[117] A. Bandyopadhyay, S. Lee, D.T. Adroja, M.R. Lees, G.B.G. Stenning, P. Aich, L. Tortora, C. Meneghini, G. Cibin, A. Berlie, R.A. Saha, D. Takegami, A. Meléndez-Sans, G. Poelchen, M. Yoshimura, K.D. Tsuei, Z. Hu, T.-S. Chan, S. Chattopadhyay, G.S. Thakur, and K.-Y- Choi, Phys. Rev. Mater. **8**, 074405 (2024)

[118] E.V. Komleva, D.I. Khomskii, and S.V. Streltsov, Phys. Rev. B **102**, 174448 (2020)

[119] G. Cao, H. Zheng, H. Zhao, Y. Ni, C.A. Pocs, Y. Zhang, F. Ye, C. Hoffmann, X. Wang, M. Lee, M. Hermele, and I. Kimchi, npj Quantum Mater. **5**, 26 (2020)

[120] Y. Shen, J. Sears, G. Fabbris, A. Weichselbaum, W. Yin, H. Zhao, D.G. Mazzone, H. Miao, M.H. Upton, D. Casa, R. Acevedo-Esteves, C. Nelson, A.M. Barbour, C. Mazzoli, G. Cao, and M.P.M. Dean, Phys. Rev. Lett. **129**, 207201 (2022)

[121] M. Ye, H.-S. Kim, J.-W. Kim, C.-J. Won, K. Haule, D. Vanderbilt, S.-W. Cheong, and G. Blumberg, Phys. Rev. B **98**, 201105(R) (2018)

[122] Y. Doi, M. Wakeshima, Y. Hinatsu, A. Tobo, K. Ohoyama, and Y. Yamaguchi, J. Mater. Chem. **11**, 3135 (2001)

[123] Y. Doi, K. Matsuhira, and Y. Hinatsu, J. Solid State Chem. **165**, 317 (2002)

[124] Y. Hinatsu and Y. Doi, Bull. Chem. Soc. Jpn. **76**, 1093 (2003)

[125] B. Yuan, B.H. Kim, Q. Chen, D. Dobrowolski, M. Azmańska, G.M. Luke, S. Fan, V. Bisogni, J. Pelliciari, and J.P. Clancy, Phys. Rev. Lett. **134**, 106504 (2025)